Title: Cryo-EM structure of endogenous *Plasmodium falciparum* Pfs230 and Pfs48/45 fertilization complex

Authors:

Melanie H. Dietrich[1,2], Jill Chmielewski[1,2], Li-Jin Chan[1,2], Li Lynn Tan[1], Amy Adair[1], Frankie M. T. Lyons[1,2], Mikha Gabriela[1,2], Sash Lopaticki[1,3], Toby A Dite[1,2], Laura F Dagley[1,2], Lucia Pazzagli[4], Priya Gupta[4], Mohd Kamil[4], Ashley M. Vaughan[4,5], Rattanaporn Rojrung[6], Anju Abraham[1], Ramin Mazhari[1,2], Rhea J. Longley[1,2,7], Kathleen Zeglinski[1,2], Quentin Gouil[1,2,8,9], Ivo Mueller[1,2,10], Stewart A. Fabb[11], Rekha Shandre-Mugan[11], Colin W. Pouton[11], Alisa Glukhova[1,2,12,13,14], Shabih Shakeel[1,2,12,14] and Wai-Hong Tham[1,2,15*]

Affiliations:

[1]The Walter and Eliza Hall Institute of Medical Research; Parkville, Australia.

[2]Department of Medical Biology, The University of Melbourne; Melbourne, Australia.

[3]Department of Infectious Diseases, Doherty Institute, University of Melbourne; Parkville, Australia.

[4]Seattle Children's Research Institute; Seattle, USA.

[5]Department of Pediatrics, University of Washington; Seattle, USA.

[6]Division of Malaria Research, Proteo-Science Center, Ehime University; Japan.

[7]Faculty of Tropical Medicine, Mahidol University; Bangkok, Thailand.

[8]Olivia Newton-John Cancer Research Institute; Heidelberg, Australia.

[9]School of Cancer Medicine, La Trobe University; Bundoora, Australia.

[10]School of Global Health, Shanghai Jiao Tong University; Shanghai, China.

[11]Monash Institute of Pharmaceutical Sciences, Monash University; Parkville, Australia.

[12]Department of Biochemistry and Pharmacology, The University of Melbourne; Melbourne, Australia.

[13]Drug Discovery Biology, Monash Institute of Pharmaceutical Sciences, Monash University; Parkville, Australia.

[14]ARC Centre for Cryo-electron Microscopy of Membrane Proteins, Monash Institute of Pharmaceutical Sciences, Monash University; Parkville, Australia.

[15]Research School of Biology, The Australian National University; Canberra, Australia.

*Corresponding author. Email: tham@wehi.edu.au

Abstract:

Malaria parasite fertilization occurs in the midgut of a female *Anopheles* mosquito. Blocking fertilization within the mosquito can prevent malaria transmission. *Plasmodium falciparum* Pfs230 and Pfs48/45 are critical for male fertility and transmission of the malaria parasite. They form a core fertilization complex, but it is unknown how they interact. We determined a cryo-electron microscopy structure of endogenous Pfs230-Pfs48/45 complex showing that Pfs48/45 interacts with Pfs230 domains 13 and 14. Transgenic parasite lines with these domains removed were defective in Pfs230 gamete localization and showed reduced oocyst formation. Nanobodies against domains 13 and 14 inhibited Pfs230-Pfs48/45 complex formation, reduced transmission and structural analyses revealed their epitopes. These Pfs230 domains were targets of naturally acquired immunity and immune sera from mRNA-LNP immunizations blocked parasite transmission.

Main Text:

Malaria causes over 600,000 deaths each year, with *Plasmodium falciparum* being responsible for almost all deaths (*1*). *P. falciparum* has a complex life cycle involving the female *Anopheles* mosquito and the human vertebrate host. Transmission-blocking vaccines are important tools to control parasite transmission from humans to mosquitos. Targeting the sexual stages of malaria parasites in the mosquito to block transmission is advantageous compared to other life cycle stages, because the development of the parasite in the mosquito entails bottlenecks in terms of parasite numbers (*2*).

Two leading transmission-blocking vaccine candidates for *P. falciparum* are Pfs230 and Pfs48/45, and both are members of the 6-cysteine protein family (*3*, *4*). Pfs230 localizes to the parasite membrane via its interaction with Pfs48/45 (*5*, *6*), which has a putative glycosylphosphatidylinositol (GPI)-anchor (*7*, *8*). Both are localized to the surface of gametocytes and gametes (*9–11*). Male *P230* gene knockouts *in P. falciparum* are unable to form exflagellation centers, in which male gametes adhere to red blood cells (*12*) and unable to recognize female gametes in *P. berghei* (*10*). When the *P48/45* gene is knocked out in *P. falciparum* and *P. berghei*, male parasites are unable to attach to female gametes, leading to reduced ookinete production (*10*, *13*, *14*). Both Pfs230 and Pfs48/45 are critical for male parasite fertility.

Full-length Pfs230, which has 14 6-cysteine domains (D1 to D14), is difficult to produce recombinantly, and so most transmission-blocking Pfs230 vaccine immunogens focus on D1 (*15–24*). Crystal structures are determined only for D1 and D2 of Pfs230 (*19*, *20*, *25–27*). Thus, whether the other 13 Pfs230 domains could function as transmission-blocking vaccine candidates is unknown. The crystal structure of the extracellular domain of Pfs48/45 has been determined (*28*) and transmission-blocking epitopes identified on all three 6-cysteine domains (*29–33*).

Here we aimed to address two key questions how does Pfs230 interact with Pfs48/45, and are there additional domains that can function as vaccine candidates to block transmission?

Cryo-EM structure of the Pfs230-Pfs48/45 fertilization complex showed the critical sites for complex formation

To investigate the structure of the Pfs230-Pfs48/45 fertilization complex, we purified the endogenous parasite proteins from late-stage sexual stage parasites and used cryo-EM for structure determination. Pfs230 is the largest member of the 6-cysteine family with 14 6-cysteine domains (D1 – D14) and a molecular weight exceeding 300 kDa, whereas Pfs48/45 has three 6-cysteine domains (*34*, *35*). We generated a *P. falciparum* transgenic line, Pfs230FL, which had Pfs230 tagged with a C-terminal 3xFLAG-TwinStrepII (fig. S1). Using affinity pulldown followed by size exclusion chromatography (SEC), we successfully isolated the Pfs230-Pfs48/45 complex (Fig. 1A and 1B). Pfs230 was present as 360 kDa and 310 kDa bands, with the lower band representing proteolytically cleaved Pfs230 (Fig. 1B). Pfs48/45 migrated at ~50 kDa as predicted from its molecular weight. Furthermore, we confirmed purification of the endogenous Pfs230-Pfs48/45 fertilization complex in multiple preparations using mass spectrometry (fig. S2).

The cryo-EM map of the endogenous Pfs230-Pfs48/45 complex was determined to a global resolution of 3.4 Å (Fig. 1C, fig. S3, fig. S4 and Table S1). However, due to the strong preferred orientation bias observed, our cryo-EM map may not contain the level of detail expected of reported global resolution. The Pfs230-Pfs48/45 fertilization complex has a 1:1 stoichiometry and is approximately 200 Å wide and 135 Å long (Fig. 1C). Pfs230 can be divided into two regions, an extended N-terminal region encompassing D1 to D8 which was determined with lower resolution in our EM map (4.6 and 9.3 Å) and a higher resolution C-terminal region consisting of D9 to D14 (3.0 to 7.2 Å), which is more compact and rigid as indicated by the local resolution

estimation (Fig. 1C, right). Due to the varying quality, we decided not to include side chains in any of our analyses.

Our cryo-EM structure revealed that all three domains of Pfs48/45 interact with Pfs230, specifically engaging with its D13 and D14 domains, with a buried surface area of 2554 Å^2 (Fig. 1C and 1D). Notably, the C-terminal end of Pfs230 extends in between Pfs48/45 D1 and D3 (Fig. 1D and 1E, panel i). Among the three 6-cysteine domains of Pfs48/45, D1 is the most well-resolved with clear density maps for ~98% of its backbone. It binds to one side of Pfs230 D14, with three of its loops (loop 1 N53-R67, loop 2 K88-F95 and loop 3 T161-G170) pointing towards Pfs230 D11 (Fig. 1E, panel ii). Pfs48/45 D2 interacts with D14 (Fig. 1E, panel iii), while D3 contacts both D13 and D14 (Fig. 1E, panel iii and iv).

The interaction of Pfs230 with Pfs48/45 was further validated using crosslinking mass spectrometry, which showed that Pfs48/45 is in close proximity to the C-terminal end of Pfs230 (Fig. 1F, fig. S5 and Data S1). Overall, 415 of 494 observed crosslinks were mapped on the structural model. Despite the high flexibility within the complex, about 82% of the crosslinks agree with the structural model with a median Cα-Cα distance of less than 20 Å (Data S1). There were four crosslinks found between Pfs230 and Pfs48/45, which were consistent with our Pfs230-Pfs48/45 cryo-EM structure. Intermolecular crosslinks with a Cα-Cα distance less than 20 Å were mapped onto the Pfs230-Pfs48/45 structure, showing that Pfs230 D14 is near Pfs48/45 D1 and D2 (indicated as black lines with orange and teal circles, Fig. 1D and 1E, panels ii and iii). Thus, Pfs230 D13 and D14 are critical domains for the interaction with Pfs48/45.

Tertiary fold of the endogenous Pfs230-Pfs48/45 complex

Our cryo-EM structure of Pfs230 contains multiple tandem pairs of 6-cysteine domains within one protein and provides an opportunity to understand how these domains form their tertiary fold (Fig. 2A). Our model comprising D1-D8 of Pfs230 is based on rigid-body fitting of predicted

structures from AlphaFold2 due to limited resolution of the map in these domains, while all other domains with sufficiently high resolution were real-space refined. We used the well-defined map of D9 - D14 to direct the placement of D7 and D8. The map quality of the region spanning D9-D14 allowed unambiguous placement of these domains. These placements in turn directed the position of tandem domains D7 and D8 because the elongated map region connected to D9 - D14 can only accommodate one tandem 6-cysteine pair. The AlphaFold-predicted model comprising D1-D6 was then placed into the remaining more globular shaped part of the map. The 14 domains of Pfs230 form seven tandem pairs of 6-cysteine domains (D1D2, D3D4, D5D6, D7D8, D9D10, D11D12 and D13D14) (Fig. 2B). At the globular level, the N-terminal (D1 - D8) and C-terminal regions (D9 - D14) of Pfs230 are arranged in an L-shaped form to each other (Fig. 2A-B). Within the N-terminal region of Pfs230, which encompasses D1 to D8, the tandem pairs D3D4 and D5D6 are arranged in a compact manner, with the four domains forming a platform on which D2 sits (Fig. 2C). Pfs230 D1 is positioned at the tip and is in contact only with D2. Furthermore, Pfs230 D7 is only in direct contact with its adjacent 6-cysteine domains D6 and D8, and D8 is only in direct contact with D7 and D9 (Fig. 2C, panel i). For the C-terminal region, Pfs230 domains D9-D14 fold into a compact and rigid arrangement involving all three tandem pairs, D9D10, D11D12 and D13D14 (Fig. 2D). Pfs230 D10, D11 and D13 form the ‘center' and are surrounded by four other 6-cysteine domains each: D10 is surrounded by D9, D11, D13 and D14; D11 is surrounded by D9, D10, D12 and D13; and D13 is surrounded by D10, D11, D12 and D14 (Fig. 2D, panel i-iii).

The two β-sandwich domains of each tandem pair are connected by a short linker and tilted against each other with varying degrees from 38° to 90° based on their center of mass (Fig. 2E). These angles provide a range that is present in tandem 6-cysteine domains and are important in how they form hetero-complexes such as in Pf12 and Pf41. We observe a similar range of

interdomain tilting from crystal structures of other 6-cysteine proteins that contain tandem pairs such as Pf12, Pf41, Pf12p and Pfs48/45 (Fig. 2F)(*25*, *36–40*).

Domains 13 and 14 of Pfs230 are critical for the localization of Pfs230 on *P. falciparum* gametes and successful parasite fertilization

Our cryo-EM structure showed that D13 and D14 of Pfs230 were required for the interaction with Pfs48/45. We thus wanted to determine if the removal of those domains would perturb Pfs230 localization on gametes. We generated a *P. falciparum* transgenic line that expressed Pfs230 without D13 and D14 (230Δ1314, Figure S6A) in a NF54/iGP2 background (*41*). Using an anti-Pfs230 monoclonal antibody (mAb) LMIV230-01 (*19*), we detected a 350 kDa band for 230FL stage V gametocytes under non-reducing conditions (Fig. 3A). In contrast, Pfs230 migrated as a lower molecular weight band in the 230Δ1314 line, which was expected due to the removal of amino acids spanning K2828 to L3135, resulting in a loss of 36 kDa. The respective bands in Pfs230FL and 230Δ1314 were also detected using anti-FLAG and anti-StrepII antibodies (Fig. 3A). Thus, Pfs230 without D13 and D14 was still expressed in late-stage gametocytes.

We initially compared the localization of Pfs230 and Pfs48/45 in stage V gametocytes between the parental NF54/iGP2 and 230Δ1314 lines. Using an immunofluorescence assay with anti-Pfs48/45 mAb TB31F (*40*) and anti-Pfs230 mAb LMIV230-01 (*19*), which were directly conjugated to Alexa647 and Alexa555, respectively, we observed colocalization of Pfs230 and Pfs48/45 in stage V gametocytes in both NF54/iGP2 and 230Δ1314 lines (Fig. 3B). However, the lattice-like pattern of Pfs230 and Pfs48/45 staining seen in the NF54/iGP2 stage V gametocytes was absent in the 230D1314 line (Fig. 3B). These immunofluorescence results showed that Pfs230 was still expressed in the 230Δ1314 line and colocalized with Pfs48/45. However, because stage V gametocytes are still within the red blood cells, we were unable to determine if Pfs230 was localized at the parasite surface without D13 and D14.

To determine if Pfs230 was localized on the surface of activated male and female gametes, we used a surface immunofluorescence assay (SIFA) (Fig. 3C and fig. S6B). As expected for NF54/iGP2, Pfs230 and Pfs48/45 were expressed and colocalized on both male microgametes and female macrogametes (Fig. 3C). In contrast, for 230Δ1314, while we observed Pfs48/45 localization on the surface of microgametes and macrogametes, there was an absence of Pfs230 on the surface of the gametes (Fig. 3C). In two independent clones of 230Δ1314, over 90% of activated female gametes had no Pfs230 localization on their surfaces compared to 14% in NF54/iGP2 (Fig. 3D and fig. S6C). Thus, D13 and D14 of Pfs230 were critical for its localization on the surface of male microgametes and female macrogametes.

We also examined if the 230Δ1314 transgenic parasites had a defect in parasite fertilization. Using the standard membrane feeding assay (SMFA), in which mosquitoes are fed with infected blood to measure effectiveness of malaria parasite transmission in the mosquito, we observed that the NF54/iGP2 line had a mean oocyst count of 87 and 24 oocysts per midgut in experiments 1 and 2 respectively (Fig. 3E). However, in two independent clones of 230Δ1314, we observed a significant reduction of oocyst formation with a mean oocyst count of 0 per midgut in both clones, and mean oocyst counts of 0.2 and 3 oocysts per midgut in experiment 2 (Fig. 3E). Thus, D13 and D14 of Pfs230 were critical for its role in parasite fertilization.

Nanobodies specific to Pfs230 D13D14 recognized gametocytes

We wanted to examine if nanobodies against Pfs230 D13D14 could inhibit Pfs230-Pfs48/45 complex formation. Using phage display, we identified 11 unique nanobodies (W2802 – W2812) using Sanger sequencing (Fig. 4A and Data S2). All these nanobodies were also identified among the top 100 most abundant sequences by Next-Generation Sequencing (NGS) (Fig. 4B and fig. S7). Seven of these nanobodies (W2806 – W2812) bound to Pfs230 D13D14 by ELISA (Fig. 4A). In addition, nanobodies F5 and F10 raised against Pfs230 D1D2 (*25*) and nanobodies

targeting other 6-cysteine proteins, such as anti-Pf12p nanobody C12 and anti-Pf41 nanobody G12, had no detectable binding to Pfs230 D13D14 (*38*, *39*) (Fig. 4A).

Of the seven Pfs230 D13D14 nanobodies, four nanobodies (W2809, W2810, W2811 and W2812) bound to recombinant Pfs230 D13D14 as determined by biolayer interferometry (BLI), with affinities from 1.6 to 46.6 nM (Fig. 4C and Data S2). W2811 and W2812 bound Pfs230 in the same epitope bin, while W2809 and W2810 bound distinct epitopes to the others (Fig. 4D). To examine the specificity of the four Pfs230 D13D14 nanobodies, we expressed and purified Pfs230 D1D2, D5D6 and D11D12, which have 20%, 18% and 22% amino acid sequence identity to Pfs230 D13D14, respectively. We also expressed the homologous D13D14 domains in Pvs230. The four anti-Pfs230 D13D14 nanobodies did not recognize Pfs230 domains D1D2, D5D6 or D11D12 or Pvs230 D13D14 by BLI (Fig. 4E). Thus, W2809, W2810, W2811 and W2812 were highly specific for Pfs230 D13D14. Staining of Pfs230 nanobodies W2810, W2811 and W2812 colocalized with anti-Pfs230 mAb LMIV230-01 staining on fixed stage V gametocytes (Fig. 4F). However, W2809 showed no detectable staining of Pfs230 in gametocytes, which suggested that its binding was sensitive to the fixation methods used. As expected, SARS-CoV-2 nanobody WNb7 (*42*) did not show any detectable staining of gametocytes (Fig. 4F).

Structural analyses of Pfs230 D13D14 nanobodies that inhibit Pfs230-Pfs48/45 complex formation and have transmission-reducing activity

To determine if anti-Pfs230 nanobodies could inhibit complex formation, we performed pull-down assays to isolate the endogenous Pfs230-Pfs48/45 complex using our transgenic 230FL line. Endogenous Pfs230-Pfs48/45 complex was pulled down using StrepTactin XT resin in the absence of any antibody, as observed in the eluate lane (lane E, no Ab) (Fig. 4G). In the presence of anti-Pfs230 mAb LMIV230-01, anti-SARS-CoV-2 nanobody-Fc fusion WNb7-Fc and anti-Pfs230 D1D2 nanobody-Fc fusion F10-Fc, we still observed the presence of the Pfs230-Pfs48/45

complex in the eluate lane, showing that these antibodies did not inhibit complex formation. In contrast, the addition of anti-Pfs48/45 mAb TB31F resulted in the loss of Pfs48/45, indicating that complex formation between Pfs230 and Pfs48/45 was disrupted (Fig. 4G). We observed a similar loss of Pfs48/45 with the addition of the anti-Pfs230 D13D14 nanobody-Fc fusions W2809-Fc, W2810-Fc, W2811-Fc and W2812-Fc, showing that these nanobodies inhibited complex formation between Pfs230 and Pfs48/45 (Fig. 4G).

To determine whether the ability of the nanobodies to block complex formation correlated with an ability to block parasite transmission, their transmission-blocking capability was assessed by SMFA. LMIV230-01 was used as a positive control and consistently showed >99% transmission-reducing activity (TRA) at a concentration of 200 µg/mL (Fig. 4H), as previously reported (*19*, *25*). PBS and WNb7-Fc were used as negative controls. At 100 µg/mL, nanobody-Fc fusion W2809-Fc reduced oocyst numbers in the mosquito across two repeat experiments, showing TRA of up to 47% (Fig. 4H, left and middle panels). However, increasing the concentration of nanobody-Fc to 200 µg/mL did not increase TRA for W2809-Fc (Fig. 4H, right panel). W2811-Fc showed TRA of between 17% and 44% across experiments; W2810-Fc did not show any TRA at 100 µg/mL but showed TRA of 43% at 200 µg/mL; and W2812-Fc did not show any TRA across experiments (Fig. 4H).

To understand the interaction of these nanobodies with Pfs230, we determined the crystal structures of the Pfs230 D13D14-W2809 complex, Pfs230 D13D14-W2810 complex and Pfs230 D13D14-W2812 complex at resolutions of 2.5 Å, 1.9 Å, and 3.2 Å, respectively (Fig. 5A and Table S2). The crystal structures showed that nanobodies W2810 and W2812 bound to D13 exclusively, whereas W2809 bound both domains, with most contacts formed with D14 (Fig. 5A, Fig. 5B and Table S3). All three nanobodies bound to non-overlapping regions, as predicted by the epitope binning experiments (Fig. 4D). W2809, W2810 and W2812 bound to Pfs230 D13D14

with a buried surface area of 711 Å^2, 588 Å^2 and 685 Å^2, respectively (Fig. 5B). The W2809 epitope overlapped where Pfs48/45 D1 predominantly engages with Pfs230 D14 (Fig. 5C). While the epitopes of W2810 and W2812 do not overlap with the Pfs230-Pfs48/45 interaction site, their binding may disrupt the conformation or interactions of D13 with neighboring Pfs230 domains, such as D12 and parts of D11 (Fig. 5C). Overlaying our cryo-EM structure of Pfs230-Pfs48/45 with the crystal structure of TB31F Fab bound to Pfs48/45 (PDB ID 6E63)(*40*) showed that the TB31F epitope overlapped with where Pfs230 D13D14 bound Pfs48/45 D3 (Fig. 5D and E).

Pfs230 D13D14 is a target of naturally acquired antibodies

To determine if Pfs230 domains are targets of naturally acquired antibodies, we used a multiplexed assay (*43*) to screen for reactivity of naturally acquired humoral immunity to Pfs230 domains and its ortholog from *P. vivax*, Pvs230, in children from Papua New Guinea (PNG) where *P. falciparum* and *P. vivax* are hyperendemic. The mean total IgG antibodies against Pfs230 D1D2, D5D6, D11D12 and D13D14 were significantly higher in PNG children than in malaria-naïve individuals (Fig. 6A and 6B). Our finding suggests that individuals living in malaria-endemic areas can develop immune responses to Pfs230 and Pvs230 through exposure to natural infections. The mean IgG levels against most constructs were notably higher in individuals with a current *P. falciparum* infection (Pf pos) as compared to those who had a prior infection (Pf prior), especially for Pfs230 D1D2 (Fig. 6B). These findings suggest that antibodies induced by natural infection may not confer long-lived immunity in the absence of recurrent infections. Our results suggest that a Pfs230 vaccine could potentially be employed as a booster to maintain high levels of Pfs230-specific antibodies, especially in areas with low malaria transmission and/or that natural infections may effectively boost vaccine-induced responses against both D1D2 and D13D14 domains. IgG antibody levels to the four different Pfs230 domains were only mildly correlated, supporting the limited evidence for cross-reactivity between these domains (fig. S9). Furthermore, the

immunoreactivity against Pv230 D13D14 in these samples with *P. falciparum* infections (Fig. 6B) indicates potential cross-reactivity between the two species, because only 13 individuals had a concurrent *P. vivax* infection.

Pfs230 D13D14 mRNA-LNP elicited high antibody titers that blocked transmission

Two mRNA constructs for Pfs230 D13D14 were formulated as lipid nanoparticles (mRNA-LNP) (Fig. 6C). The first mRNA encompassed a longer fragment from K2828-L3135 (230D13D14L) and the second encompassed a shorter fragment of Pfs230 D13D14 from K2828-E3111 (230D13D14S). Both constructs had a N-terminal secreted alkaline phosphatase signal peptide **(**SEAP) but no added transmembrane domain or GPI anchor. 230D13D14L and 230D13D14S mRNA-LNPs were used to immunize BALB/c mice and immune sera were assayed for antibody responses against recombinant Pfs230 D13D14 (Fig. 6C and fig. S8). After the first immunization, 230D13D14L and 230D13D14S elicited end point antibody titers of 1787 and 3824, respectively. Administration of the second immunization of both constructs resulted in significant boosting of antibody titers 80-fold and 74-fold, with 230D13D14L and 230D13D14S eliciting end point antibody titers of 144263 and 284235, respectively (Fig. 6C). Insect cell expression of Pfs230 D13D14L showed a higher proportion of aggregated protein compared to Pfs230 D13D14S (fig. S9), potentially affecting its end point titers. As expected, we did not observe any immune response to Pfs230 D13D14 in the pre-immune sera from both sets of mice, showing that the mRNA-LNP immunizations were directly responsible for the generation of Pfs230-specific antibodies (fig. S8).

Due to the limited volume of sera collected, sera from the second bleed of each mouse were pooled to determine specificity of the antisera to parasite material. Using pooled sera from the 230D13D14S mRNA-LNP immunizations, we detected a 360 kDa band in 230FL stage V gametocytes under non-reducing conditions (Fig. 6D, middle panel). In contrast, we did not detect

any band in the 230Δ1314 line, showing that the antibodies elicited by 230D13D14S mRNA-LNP immunization are completely specific to D13D14 of Pfs230. As a control, mAb LMIV230-01 which binds to Pfs230 D1 could detect the 360 kDa band in 230FL stage V gametocytes and a lower molecular weight band in the 230Δ1314 line under non-reducing conditions (Fig. 6D, right panel). Pre-immune mouse sera did not detect any band in either 230FL or the 230Δ1314 line (Fig. 6D, left panel) showing that the antibodies against Pfs230 D13D14 were elicited via mRNA-LNP immunization.

The pooled sera from the 230D13D14S mRNA-LNP immunization were able to detect Pfs230 on both stage V gametocytes using an immunofluorescence assay (Fig. 6E, bottom left panels) and the surface of macrogametes using SIFA (Fig. 6F, bottom panels). However, the pooled immune sera did not detect Pfs230 in the 230Δ1314 clonal lines (Fig. 6E, bottom right panels), again demonstrating the specificity of antibodies against D13 and D14 elicited by immunization. The anti-Pfs230 D13D14 sera staining pattern colocalized with that of the anti-Pfs230 mAb LMIV230-01 in wild-type NF54/iGP2 (Fig. 6E and 6F). As expected, the pooled pre-immune sera did not show any detectable staining of stage V gametocytes or macrogametes (Fig. 6E and 6F, top panels).

SMFAs were performed using the sera pooled from mice immunized with 230D13D14S or 230D13D14L mRNA-LNP to determine whether antibodies generated could reduce transmission. In two experiments, we observed anti-Pfs230 D13D14S sera reduced transmission by 97 and 98% when compared to pre-immune sera (Fig. 6G, experiment 1 and 2), whereas anti-Pfs230 D13D14L showed no reduction in transmission activity. In a third experiment, we included complement active human serum to assess how complement would affect transmission blocking activity. Here we observed similar results to the SMFA performed without active human complement. SMFA with pre-immune serum had a mean of 24 oocysts per midgut and the addition

of anti-230D13D14S sera in the presence of active human complement reduced transmission by 99.7% (Fig. 6G, experiment 3). Thus, 230D13D14S mRNA-LNP immunization elicited Pfs230 D13D14-specific antibodies that significantly reduced parasite transmission independent of active human complement.

Discussion

Our cryo-EM structure of the Pfs230-Pfs48/45 fertilization complex identified Pfs230 D13D14 as important for Pfs230's interaction with Pfs48/45. Using a transgenic *P. falciparum* line that expressed Pfs230 without D13 and D14, we showed that the presence of these domains was critical for the localization of Pfs230 on the surface of gametes and for successful parasite fertilization. Nanobodies against Pfs230 D13 and D14 inhibited Pfs230-Pfs48/45 complex formation, and several reduced oocyst formation in the mosquito midgut. Crystal structures of the inhibitory nanobodies bound to Pfs230 D13D14 provided mechanistic insights on future approaches to develop more potent transmission-blocking antibodies. Pfs230 D13D14 was a target of naturally acquired immunity in PNG children with current and prior *P. falciparum* infection. In addition, we showed that a 230D13D14S mRNA-LNP immunogen elicited Pfs230 D13D14-specific antibodies capable of reducing transmission in mosquitoes.

A *P. falciparum* transgenic line that did not express D13D14 had a strong defect in surface localization of Pfs230 in activated male and female gametes compared with the parental line. Using independent clones of 230ΔD1314, we showed that over 90% of activated female gametes had no Pfs230 localization on their surfaces compared to 14% in NF54/iGP2. This phenotype was similar to the absence of Pfs230 on activated gametes observed for a Pfs48/45 knockout line (*12*). In addition, 230Δ1314 parasites were defective in parasite fertilization as observed by the significant decrease in oocyst development in the mosquito midgut compared to the parental line. These

results showed that D13 and D14 of Pfs230 are critical for its function and provides a novel immunogen for transmission blocking vaccines.

Our nanobodies are specific to Pfs230 D13D14. Over 20 inhibitory monoclonal antibodies targeting *P. falciparum* Pfs230 have been reported, with transmission-reducing activities ranging from 42% to 100% (*9*, *11*, *17*, *19*, *20*, *25*, *44–48*). All these monoclonal antibodies bind to Pfs230 D1, except for 18F25.1, which binds to Pfs230 D7. Our nanobody W2809, when fused to a human IgG1 Fc domain, showed transmission reduction of up to 47% at a concentration of 100 µg/mL. However, it had the lowest affinity to Pfs230 D13D14, with a K_D of 46.6 nM. Future nanobody engineering approaches using information from our high-resolution crystal structures may yield a higher affinity nanobody to Pfs230 D13D14, which could improve its transmission-blocking potency. Nanobody W2811 showed up to 44% reduction in transmission when assessed by SMFA. Nanobody W2811 and W2812 bound in the same epitope bin and had similar affinities for Pfs230 D13 but W2812 had negligible transmission-blocking capabilities. To improve the potency of nanobody W2811, understanding its precise epitope using X-ray crystallography will be required.

Our Pfs230 D13D14 mRNA-LNP immunogens elicited antibodies specific to these Pfs230 domains. However, only immunization with 230D13D14S mRNA-LNP generated antibodies that potently reduced transmission up to 98%. Currently, we do not fully understand why 230D13D14L mRNA-LNP immunization did not generate transmission blocking antibodies. We did observe that Pfs230 D13D14S induced ~ 2x more antibody end point titers compared to Pfs230 D13D14L. Furthermore, our insect cell expression of Pfs230 D13D14L showed a higher proportion of aggregated protein compared to Pfs230 D13D14S. We propose that the lower titers and potential presence of more aggregated protein for Pfs230 D13D14L may have affected its ability to elicit antibodies with transmission-blocking activity. A recent study on Pfs25 and Pfs230D1 shows that mRNA constructs with a GPI anchor or transmembrane domain generates sera with higher

transmission-blocking activity (*49*). Next generation designs for Pfs230 D13D14 should include a signal peptide and either a GPI anchor or transmembrane domain to determine whether membrane anchorage also elevates antibody titers using our mRNA-LNPs. Future studies should examine if a combination of mRNA-LNP vaccine encoding Pfs48/45 and the most potent fragment of Pfs230 will provide a higher transmission-reducing functional activity compared to with individual subunit vaccines.

Collectively, our results showed that Pfs230 D13D14 is a promising transmission-blocking vaccine candidate. Furthermore, our cryo-EM structure showed that D14 of Pfs230 engaged with all three Pfs48/45 domains, therefore D14 alone showed promise as a target of transmission-blocking antibodies or for the development of a smaller subunit vaccine. In addition, nanobody W2809 which bound mostly to Pfs230 D14, blocked Pfs230-Pfs48/45 complex formation and reduced transmission by up to 47%. In the last 30 years, most Pfs230 vaccine immunogens focus on the development of D1, in part driven by its ability to generate potent transmission-blocking antibodies and the ease of recombinant protein expression for this domain (*15–24*). Our comprehensive structural analyses of the endogenous Pfs230-Pfs48/45 fertilization complex and Pfs230-nanobody complexes will facilitate future rational design of vaccines and transmission-blocking monoclonal antibody approaches.

Materials and methods

Generation of transgenic Pfs230FL and 230Δ1314 3xFLAG-TwinStrepII-tagged parasites

To introduce 3xFLAG-TwinStrepII tag to the C-terminal end of Pfs230, we used the NABS4_3xFLAG-TwinStrepII_5'-3'_Pfs230 construct. This construct was generated as follows: 3xFLAG-TwinStrepII was synthesized as a gBlock (Integrated DNA Technologies) and cloned into the NABS4 vector using XhoI/XmaI. A 5' homology region (HR1) of Pfs230 followed by a

recodonized coding sequence was cloned into the NABS4_3xFLAG-TwinStrepII plasmid using NotI and XhoI restriction sites. Subsequently the 3' homology region (HR2) for targeting Pfs230 was cloned in using KpnI and PstI sites.

A Cas9/guide RNA expressing plasmid (*50*) with guide sequence targeting Pfs230 (pUF1-Cas9_Pfs230_g8947) was transfected with NotI and PstI linearized NABS4_3xFLAG-TwinStrepII_5'-3'_Pfs230 into NF54/iGP2 parasites (*41*), using the Lonza Nucleofector Transfection 2b device and Basic Parasite Nucleofector Kit 2 as previously described (*51*). In brief, synchronized schizonts were purified using a Percoll (Cytiva) density gradient. 100 µg each of the linearized repair template and Cas9/guide expressing plasmid pUF1-Cas9_Pfs230_g8947 was resuspended in 100 µL of supplemented Basic Parasite Nucleofector Solution 2. 50 µL of packed schizonts were resuspended in the DNA/Nucleofector solution and transferred to the cuvette for electroporation (program U-33). Electroporated parasites were transferred to a prewarmed 1.5 mL Eppendorf tube using 500 µL of culture medium and 50 µL of fresh red blood cells and incubated at 37 °C at 650 RPM for 30 mins. Transfected parasites were returned to regular culture conditions. The following day, 2.5 nM of the selection drug WR99210 (Jacobus Pharmaceutical Co) was added and maintained until >2% parasitemia was observed.

To generate the 230Δ1314 line, NABS4_3xFLAG-TwinStrepII_5'-3'_Pfs230 was modified in the following way. The nucleotide sequence 5' of D13 of Pfs230 was PCR amplified to use as the 5' homology region (HR3) and cloned into the vector using NotI and XhoI sites, and this plasmid is called NABS4-3xFLAG TwinStrepII_Pfs230_3'_D13D14_5'. Parasite transfection with this construct was performed as described above with the same Cas9/guide RNA expressing plasmid pUF1-Cas9_Pfs230_g8947. Clonal parasite populations were obtained using limited dilution cloning. Parasites were assessed for integration of the 3xFLAG-TwinStrepII tag at the 3' of the gene by extracting gDNA from 0.15% saponin lysed parasite material (DNeasyBlood and

Tissue Kit, Qiagen) and using genotyping PCR (CloneAmp HiFi PCR premix, Takara). In addition, immunoblotting was used to confirm the expression of the 3xFLAG-TwinStrepII tag on Pfs230 (fig. S1C). All primer and synthetic DNA sequences are provided in Table S4.

Asexual blood stage growth and gametocyte development

Asexual *P. falciparum* parasite cultures were maintained with O^+ red blood cells at 4% haematocrit in RPMI 1640, GlutaMAX, HEPES (Thermo Fisher) supplemented with: hypoxanthine (12.5 mg/L) (Sigma), D-glucose (2 g/L) (Thermo Fisher), gentamycin (20 mg/L) (Thermo Fisher), 0.25% (w/v) AlbuMAX II (Thermo Fisher), and 5% (v/v) O^+ human serum (Australian Red Cross, Lifeblood). Cultures were maintained by routine sub-culturing and media replacement as necessary, and NF54/iGP2 maintained as asexual forms through the addition of 2.5 mM D-(+)-glucosamine hydrochloride (Sigma). Gametocytes were induced as previously described for the NF54/iGP2 line (*41*) and when the culture was majority stage V gametocytes, they were maintained at 37°C until red blood cells were lysed using 0.03% saponin. Parasites were washed in ice cold phosphate buffered saline (PBS) supplemented with cOmplete protease inhibitor (Roche) and stored at -80°C until protein purification.

Purification of endogenous Pfs230-Pfs48/45 complex from stage V gametocytes

Parasite pellets were resuspended in lysis buffer, comprising 50 mM HEPES pH 8.0, 150 mM NaCl, 10 mM EDTA pH 8, 10% (v/v) glycerol, and either 1% *n*-dodecyl β-D-maltoside (DDM) or glyco-diosgenin (GDN), and incubated at room temperature (RT) for 45 min on rollers. The soluble lysate was separated from the insoluble fraction by centrifuging at 16,000 *x* g for 1 h at 4°C and incubated with StrepTactin XT resin (IBA Lifesciences, equilibrated in lysis buffer) for 2 h on rollers at 4°C. The resin was transferred to a gravity chromatography column and washed with wash buffer containing reduced detergent concentrations. Elution was performed with 1x Buffer BXT (IBA Lifesciences) containing 5% (v/v) glycerol and 0.02% DDM or 0.0075% GDN

in addition to 100 mM Tris-HCl pH 8.0, 1 mM EDTA and 50 mM biotin. Fractions containing the proteins of interest were pooled and concentrated using a 30 kDa molecular weight cutoff (MWCO) Millipore concentrator. Size exclusion chromatography (SEC) was used to assess sample quality and as a last purification step. The sample was applied to a Superose 6 3.2/300 column (Cytiva) equilibrated in 50 mM HEPES pH 8.0, 150 mM NaCl, 3% (v/v) glycerol, 0.02% DDM or 0.0075% GDN. Samples from fractions of interest, alongside 1 µg SARS-CoV-2 Spike (*42*), were loaded onto a 3-8% NuPAGE Tris-Acetate gel (Invitrogen) and run in 1X Tris-Acetate running buffer for 1 h at 150 V. Gels were stained with InstantBlue Coomassie protein stain to identify fractions containing the complex. Protein in DDM-containing buffer was used for cryo-EM and the protein in GDN for crosslinking-mass spectrometry approaches.

Purification of recombinant Pfs230 domains

Codon optimized (*Spodoptera frugiperda, Sf*) DNA corresponding to amino acids K2828-E3111 of Pfs230 (D13D14), D2446-T2818 of Pfs230 (D11D12), T1281-G1549 of Pfs230 (D5D6) and N2450-S2731 of Pvs230 (PvD13D14) were cloned into a modified form of baculovirus transfer vector pAcGP67-A. The Pfs230 sequence is in frame with the GP67-signal sequence and an N-terminal octa-histidine tag followed by a Tobacco Etch Virus (TEV) protease cleavage site. The recombinant protein was produced using *Sf*21 cells (Life Technologies) cultured at 28°C in Insect-XPRESS Protein-free Insect Cell Medium supplemented with L-glutamine (Lonza). A cell culture of ~1.5 - 2.0 x 10^6 cells/mL was inoculated with the third passage stock of virus and incubated for three days at 28°C. Cells were separated from the supernatant by centrifugation at 17,000 *x* g for 30 min. The supernatant was sterile filtered with 0.45 µm filters and concentrated via tangential flow filtration using a 10 kDa MWCO cassette (Millipore). The concentrated supernatant was sterile filtered with a 0.45 µm filter and dialyzed into 30 mM Tris-HCl pH 7.5, 300 mM NaCl. The dialyzed sample was incubated with Ni-NTA resin (Qiagen) for 1h at 4 °C on

a roller shaker. Ni-IMAC using a gravity flow chromatography column was performed. The resin was washed with 10-20 column volumes of 30 mM Tris-HCl pH 7.5, 300 mM NaCl, followed by further washes with stepwise increases in imidazole concentration. TEV protease was added to the pooled fractions containing Pfs230 D13D14 while dialyzing into 30 mM Tris-HCl pH 7.5, 300 mM NaCl to remove the N-terminal tag. The solution was incubated with Ni-NTA resin (Qiagen) for 1h at 4°C on a roller shaker before untagged Pfs230 D13D14 was separated from His-tagged TEV protease and un-cleaved protein via Ni-IMAC purification. The flow-through was concentrated and applied to a Superdex 200 Increase 10/300 SEC column (Cytiva) pre-equilibrated with 20 mM HEPES pH 7.5, 150 mM NaCl.

Cryo-EM sample preparation and data acquisition

Cryo-EM grids were prepared using a multiple blotting approach to concentrate the particles in the holes. The main SEC peak fraction was used and 3.5 µL of sample was applied to a plasma-cleaned R1.2/1.3 UltrAuFoil grid, followed by blotting of the grid at a force of 3 N for 4 s. Four to six applications were performed, with the last blotting performed for 7 s before plunge freezing the grid in liquid ethane using a Vitrobot Mark IV (ThermoFisher) at 20 °C and 100 % humidity. Cryo-EM grids were screened on the Arctica and subsequently imaged on a Titan Krios microscope at the Ian Holmes Imaging Centre, Bio21 (IHIC, Melbourne) operated at 300 kV using a Falcon 4 detector in electron counting mode. A total of 35,375 movies were collected from four grids at a pixel size of 0.808 Å/pixel, with a total dose of 50 $e^-/Å^2$. Images were acquired using a 70 µm objective aperture and a defocus range of -0.4 to -1.6 µm.

Data processing

Movies were motion corrected and contrast transfer function parameters estimated in cryoSPARC v4.6.0 (*52*) (fig. S3 and fig. S4). Datasets from each grid were pre-processed individually. Approximately 100 particles were manually picked from each set of micrographs

before blob tuner picking in cryoSPARC. The picked particles were extracted (360 pixels, 2x binned to 180 pixels) and subjected to two-dimensional (2D) classification separately. Several rounds of 2D-classification were performed and particles from poorly defined 2D-classes iteratively excluded. About 20,563 particles of grid 1 were used for *ab initio* reconstruction into four classes. Particles of grids 1 and 2 were combined and subjected to homogenous refinement, further rounds of 2D-classification and heterogeneous refinement, which separated the particles into intact Pfs230-Pfs48/45 complex (53,851 particles) and junk (19,570 particles). Particles of grid 3 and 4 (97,225 particles) were added and further rounds of 2D-classification and heterogenous refinement used to clean up the particle stack. Particles were re-extracted (360 pixels) and subjected to local per-particle contrast transfer function (CTF) refinement. Following heterogenous refinement, a final non-uniform refinement with the final dataset of 87,061 particles yielded a consensus map of 3.36 Å based on the gold standard Fourier shell correlation (FSC) cutoff of 0.143.

To improve the density of the Pfs230 domains D1-D8, the map was subjected to a focused refinement, resulting in an overall resolution of 4.86 Å. Our consensus and local refinement cryo-EM maps of the Pfs230-Pfs48/45 complex showed preferred orientation bias, therefore, to aid in model building, we used EMReady (v2.0)(*53*) on unsharpened maps for better interpretation of the maps. We tried different values for the flag "Stride", which controls the step of the sliding window for cutting the input map into overlapping boxes that range from 12 to 48 but found the default setting of 12 worked the best. The interpretability of the consensus cryo-EM map improved for the region spanning Pfs230 D9-14 and Pfs48/45, allowing confident tracing of the backbone in most regions.

A composite map was generated from the EMReady processed consensus map and the local refinement map comprising Pfs230 D1-D8. Local resolution of the maps was estimated in

cryoSPARC (v4.6.0)(*52*). Due to the observed variations in local resolution and preferred orientation, we report only the global positions of individual domains that could be modelled with high confidence.

Model building and refinement

AlphaFold2 (*54*) and AlphaFold Multimer (v2.3.2)(*55*) predicted models of Pfs230 D1-D6 (residues 527-1683), Pfs230 D7D8 (residues 1684-2037) and Pfs230 D9-D14 (residues 2038-3133) were calculated using the WEHI high-performance computing system. The highest scoring model of the Pfs230-Pfs48/45 complex was used for model building into the composite map. The model was divided into three regions. Regions spanning Pfs230 D1-D6 (residues 527-1683), Pfs230 D7D8 (residues 1684-2037) and Pfs230 D9-D14 (residues 2038-3133)-Pfs48/45 (residues 28-428) were rigidly fitted independently into the map using ChimeraX (v1.8)(*56*). Namdinator (*57*), a web-based automated molecular dynamics based flexible fitting program, was used to improve initial fitting of the models. The Pfs230 D1-D8 model was in the lower resolution part of the map; therefore, all side chains were truncated and no further fitting was performed, except rigid body fitting in Phenix (v1.21.1)(*58*) to generate the model-map statistics (Table S1). The Pfs230 D9-D14-Pfs48/45 model was in the higher resolution part of the map. To further improve the fitting, an iterative refinement in Coot (*59*) and Phenix (with global minimization and secondary structure restraints) was performed. Side chains were truncated where the resolution was not sufficient to assign them confidently. Since our cryoEM maps have regions of preferred orientation, we only fitted the global orientation of the domains that we can model confidently. Crystal structures of the Pfs48/45 ectodomain (PDB IDs 7ZXG and 7ZXF) were used to aid model building of its domains D2 and D3 in the map.

Crosslinking mass spectrometry sample preparation and analysis

Sulfosuccinimidyl 4,4'-azipentanoate (Sulfo-SDA) (Thermo Scientific Pierce) was dissolved freshly in 50 mM HEPES pH 8.0, 150 mM NaCl, 5% (v/v) glycerol, 0.0075% GDN to a concentration of 1 mg/mL. Crosslinking reactions were performed with a two-fold dilution series of Sulfo-SDA ranging from 1.0 mg/mL to 0.06 mg/mL. Purified Pfs230-Pfs48/45 complex (5 µL, ~0.1 mg/mL, ~1.25 µM) was mixed with 5 µL Sulfo-SDA and incubated in the dark at RT for 30 min. To activate Sulfo-SDA, the samples were irradiated with an UV mercury-xenon arc lamp at 1000 watts on ice for 1 min. Crosslinked samples were analyzed on a 3-8% NuPAGE Tris-Acetate gel (Invitrogen). Protein without crosslinker and protein mixed with the highest crosslinker concentration, which lacked UV exposure, were used as controls. Gel bands corresponding to the crosslinked Pfs230-Pfs48/45 heterodimer were excised and enzymatically digested with trypsin as previously described (*60*).

Reconstituted peptides were analyzed on an Orbitrap Eclipse™ Tribrid mass spectrometer that is interfaced with a Vanquish Neo liquid chromatography system. Samples were loaded onto a C18 fused silica column (inner diameter 75 µm, OD 360 µm × 15 cm length, 1.6 µm C18 beads) packed into an emitter tip (IonOpticks) using pressure-controlled loading with a maximum pressure of 1,500 bar, which is interfaced to an Orbitrap Eclipse™ Tribrid (Thermo Scientific) mass spectrometer using EASY-nLC source and electrosprayed directly into the mass spectrometer. Peptides were eluted using a 120-minute linear gradient of 3% to 30% of acetonitrile into the mass spectrometer operating in data-dependent mode (scan parameters detailed in Data S1).

Raw data files were converted to MGF files using msConvert (*61*). MGF files were searched against a fasta file containing the Pfs230 and Pfs48/45 sequences using xiSEARCH software (version 1.7.6.7)(*62*) with the following settings: crosslinker = multiple, SDA and noncovalent; fixed modifications = Carbamidomethylation (C); variable modifications = oxidation

(M), sda-loop (KSTY) DELTAMASS:82.04186484, sda-hydro (KSTY) DELTAMASS:100.052430; MS1 tolerance = 6.0ppm, MS2 tolerance = 20.0ppm; losses = H_2O,NH_3, CH_3SOH, CleavableCrossLinkerPeptide:MASS:82.04186484). False discovery rate estimation was performed with the in-built xiFDR set to 5%. Data were visualized using the xiVIEW software(*63*).

Immunofluorescence assay on *Plasmodium falciparum* parasites

NF54/iGP2 stage V gametocytes were cultured as described above. Thin blood smears were made on glass slides, fixed in equal parts of ice-cold acetone and methanol for 10 min and allowed to air dry. The slides were incubated with 3% (w/v) bovine serum albumin (BSA)/PBS for 1 h then washed three times in 1x PBS prior to addition of the primary antibodies. The primary antibodies or nanobodies were diluted in 3% BSA/PBS. Anti-Pfs230 LMIV230-01 directly conjugated to Alexa Fluor 555 was used at a final concentration of 7.5 to 10 µg/ml, anti-Pfs48/45 TB31F directly conjugated to Alexa Fluor 647 at final concentration 7.5 to 10 µg/mL, the Pfs230 D13D14 nanobodies W2809, W2810, W2811 and W2812 and the negative control SARS-CoV-2 nanobody WNb7 were used at 4 µg/mL (*42*). Primary antibodies were incubated on the slide for 2 h within a humidified chamber. After washing as described, goat anti-alpaca IgG VHH domain conjugated to Alexa Fluor 488 (Jackson ImmunoResearch) (diluted 1:1000 in 3% BSA/PBS) was used as a secondary antibody and incubated for 2 h within a humidified chamber. For the mouse serum IFA, pooled serum was diluted to 1:500 and donkey anti-mouse conjugated to Alexa Fluor 647 (Thermo Scientific) diluted 1:1000 in 3% BSA/PBS was used as a secondary antibody. The slides were mounted with a coverslip using VECTASHIELD PLUS antifade mounting medium with DAPI (Vector Laboratories) and sealed with nail polish. Images were acquired on a Zeiss LSM 980 using confocal mode with a 63x (1.4NA) objective lens with oil immersion using the

405, 488 and 561 lasers. Images were processed using FIJI ImageJ software (v2.14.0/1.54)(*64*) and the Z-projection max intensity images were used in the figures.

Surface immunofluorescence assay of *P. falciparum* activated gametes

Stage V gametocytes were purified from uninfected red blood cells using a Percoll (Cytiva) centrifugation density gradient. Gamete activation was induced by incubation in ookinete medium (RPMI with 100 μM xanthurenic acid)(*65*) at RT for 30 min. To obtain macrogamete images, gametes were washed 3X with 0.5% fetal bovine serum (FBS), 0.05% sodium azide in PBS prior to incubation with anti-Pfs48/45 TB31F directly conjugated to Alexa Fluor 647 and anti-Pfs230 LMIV230-01 directly conjugated to Alexa Fluor 555. Antibody incubation was performed at 4ºC in the dark with gentle shaking for 1 h. Activated gametes were washed as described above, then fixed by resuspension in 2% formaldehyde in PBS for 20 min. A final series of washes was performed prior to adherence of gametes to a 0.1 mg/mL erythroagglutinin PHA-E (Sigma-Aldrich) coated coverslip. Slides were then mounted and imaged as described above using the 405, 561 and 639 lasers. Microgamete SIFA was performed by resuspending stage V gametocytes in ookinete medium supplemented with the Alexa Fluor conjugated antibodies. The activating gametes were then allowed to settle onto coverslip, incubated in a humidified chamber in the dark for 30 minutes, then fixed, mounted, and imaged as described above. Z-projection images were generated in FIJI ImageJ and brightness and contrast were adjusted for visualization. Automated quantitation of SIFA of macrogametes were performed as follows. Cell segmentation was performed via a custom trained cellpose (*66*, *67*) network on maximum intensity projected brightfield images. Cell scoring was performed via a custom FIJI (*64*) macro with manual thresholds set for mean intensity of maximum intensity projected images of 647 and 555 channels. Mask images showing the segmentation and scoring of each cell were produced for manual validation.

Immunoblotting

Parasite lysate was resuspended in either reducing or non-reducing sample buffer and separated on a 3 – 8% NuPAGE Tris-Acetate SDS-PAGE (ThermoFisher Scientific). Samples were transferred onto PVDF membranes (iBlot™ 2 Transfer Stacks, ThermoFisher Scientific) and blocked overnight in 10% skim milk in PBST. Blots were probed with anti-Pfs230 LMIV-230-01 and anti-FLAG followed by the appropriate secondary antibodies conjugated to HRP, and anti-Strep-HRP. Chemiluminescence was detected using SuperSignal West Pico PLUS Chemiluminescent Substrate (ThermoFisher Scientific). The HRP signal was inactivated using 0.025% sodium azide in PBST and re-probed with anti-HSP-70 followed by appropriate secondary and imaged as above.

Alpaca immunization and isolation of Pfs230 D13D14 nanobodies

One alpaca was immunized six times with approximately 200 µg of recombinant Pfs230 D13D14 protein on days 0, 14, 21, 28, 35 and 42. The adjuvant used was GERBU FAMA. Immunization and handling of the alpacas for scientific purposes was approved by Agriculture Victoria, Wildlife & Small Institutions Animal Ethics Committee, project approval No. 26-17. Blood was collected three days after the last immunization for the preparation of lymphocytes. Nanobody library construction was carried out according to established methods as described (*68*). Briefly, alpaca lymphocyte mRNA was extracted and amplified by RT-PCR with specific primers to generate a cDNA nanobody library. The library was cloned into a pMES4 phagemid vector containing 10^4 unique nanobodies, amplified in *E. coli* TG1 strain and subsequently infected with M13K07 helper phage for recombinant phage expression. Biopanning for recombinant Pfs230 D13D14 nanobodies using phage display was performed as previously described with the following modifications (*42*). Phages displaying Pfs230 D13D14-specific nanobodies were enriched after two rounds of biopanning with 1 µg of immobilized Pfs230 D13D14 complex. After

the second round of panning, we screened 94 clones from round two by ELISA and selected positive hits for further analysis. Positive clones were sequenced and annotated using PipeBio. Distinct nanobody clonal groups were identified based on differences in the amino acid sequence of the complementary determining region 3 (CDR3) that vary by at least one amino acid.

Purification of nanobodies and Fc-tagged nanobodies

Nanobodies were expressed in *Escherichia coli* WK6 cells and purified as previously described (*25*). Briefly, bacteria were induced at an OD_{600} of 0.7 with 1 mM IPTG and grown overnight at 28°C. Cell pellets were harvested, resuspended in 20% (w/v) sucrose, 20 mM imidazole pH 7.5, 150 mM NaCl PBS and incubated for 15 min on ice. 5 mM EDTA pH 8.0 was added followed by an incubation on ice for 20 min. After this incubation, 10 mM $MgCl_2$ was added, and periplasmic extracts were harvested by centrifugation. The supernatant was loaded onto a 1 mL HisTrap Excel column (GE Healthcare), washed and the nanobodies eluted with 400 mM imidazole pH 7.5, PBS, before being concentrated and buffer exchanged into PBS.

Nanobody sequences of W2809, W2810, W2811 and W2812 were subcloned into a derivative of pHLSec containing the hinge and Fc region of human IgG1 to produce nanobody-Fc tagged fusion proteins in Expi293 cells via transient transfection. Restriction-ligation cloning with PstI and BstEII restriction enzymes was used to introduce the respective sequences. The supernatant was harvested six days after transfection and applied to 1 mL HiTrap Mab Select PrismA affinity columns (Cytiva). Nanobody-Fcs were eluted in 100 mM citric acid pH 3.0, neutralized by the addition of 1 M Tris-HCl pH 9.0 and subsequently buffer exchanged into PBS.

Next-generation sequencing and analyses of nanobody phage libraries

Plasmids from phage libraries were digested and gel purified to isolate the nanobody domain sequences. Paired-end 2x300 bp sequencing libraries were prepared using the NEBNext Multiplex Oligos for Illumina (Cat # E7395) in a PCR-free manner according to the manufacturer's

instructions. The samples were size-selected using AMPure XP beads, quantified by qPCR using the KAPA Library Quantification Kit and sequenced on an Illumina NextSeq 2000 instrument. Raw sequencing reads were trimmed to remove sequencing adapters with TrimGalore v0.6.7 (https://github.com/FelixKrueger/TrimGalore) and then merged using FLASH v1.2.11(*69*). Annotation of nanobody sequences was performed using IgBLAST v1.19.0(*70*) with an alpaca reference database built from IMGT (*71*). Nanobody sequences were collapsed into clones at the CDR3 level, and the counts of clones were normalized through conversion to counts per million (CPM). Cladograms were generated from generalized Levenshtein distances between CDR3s with the Neighbor-Joining method(*72*) from the phangorn (v2.12.1)(*73*) package and plotted using the ggtree (v3.14.0)(*74*) package in R (v4.4.1)(*75*). Amino acid logos were made using the ggseqlogo R package (v0.2.0)(*76*).

ELISA for nanobody binding

The 96-well flat-bottomed MaxiSorp plates were coated with 125 nM of recombinant protein, as indicated, in 50 µL PBS at RT for 1 h. All washes were done three times using PBS and 0.05% (v/v) Tween-20 (PBST), and all incubations were performed for 1 h at RT. Coated plates were washed and blocked by incubation with 10% (w/v) skim milk solution. Plates were washed and then incubated with nanobody at a concentration of 125 nM. The plates were washed and incubated with mouse anti-His antibody (Bio-Rad MCA-1396; 1:1000) followed by horseradish peroxidase–conjugated goat anti-mouse secondary antibody (MerckMillipore AP124P, 1:1000). After a final wash, 50 µL azino-bis-3-ethylbenthiazoline-6-sulfonic acid (ABTS liquid substrate; Sigma 11684302001) was added and incubated in the dark at RT, and 50 µL 1% (w/v) sodium dodecyl sulfate (SDS) was used to stop the reaction. Absorbance was read at 405 nm, and all samples were done in duplicate.

Affinity determination, epitope binning and domain specificity using biolayer interferometry (BLI)

Affinity determination measurements were performed on the Octet RED96e (FortéBio). Assays using monomeric nanobodies were performed using Penta-His antibody capture sensor tips (Octet®HIS1K). For assays using nanobody-Fcs, anti-hIgG Fc capture sensor tips (Octet® AHC) were used. All measurements were performed in kinetics buffer (DPBS pH 7.4 supplemented with 0.1% (w/v) BSA and 0.05% (v/v) Tween-20) at 25°C. After a 60 s baseline step, nanobodies or nanobody-Fcs (5 µg/mL) were loaded onto sensors until a response of 0.5 nm, followed by a 60 s baseline step. Association measurements using nanobodies were performed using a two-fold dilution series of untagged Pfs230 D13D14 from 6 to 200 nM for 180 s for determination of affinity to D13D14 and a single 100 nM concentration of Pfs230 domains to determine domain specificity of nanobodies. Dissociation was measured in kinetics buffer for 180 s. Sensor tips were regenerated using five cycles of 5 s in 100 mM glycine pH 1.5 and 5 s in kinetics buffer for both HIS1K-sensors and AHC-sensors. Baseline drift was corrected by subtracting the response of a nanobody-loaded sensor incubated in kinetics buffer only. Curve fitting analysis was performed with Octet Data Analysis 10.0 software using a global fit 1:1 model to determine K_D values and kinetic parameters. The mean kinetic constants reported are the result of two to three independent experiments. Our data shows R^2 values of > 0.998 and χ^2 < 0.5 representing a statistically reliable goodness-of-fit of experimental data against the expected binding model (Dataset S2).

For epitope binning experiments, 50 nM untagged Pfs230 D13D14 was pre-incubated with each nanobody at a 10-fold molar excess for 1 h at RT. A 30 s baseline step was established between each step of the assay. The NTA sensors were first loaded with 10 µg/mL of nanobody for 5 min. The sensor surface was then quenched by dipping into 10 µg/mL of an irrelevant nanobody for 5 min. Nanobody-loaded sensors were then dipped into premixed solutions of Pfs230

D13D14 and nanobody for 5 min. Nanobody-loaded sensors were also dipped into Pfs230 D13D14 alone to determine the level of Pfs230 D13D14 binding to immobilized nanobody in the absence of other nanobodies. Percentage competition was calculated by dividing the max response of the premixed Pfs230 D13D14 and nanobody solution binding by the max response of Pfs230 binding alone, multiplied by 100.

Pull-down assay of endogenous Pfs230-Pfs48/45 complex for blocking nanobodies

Parasite lysates for the pull-down assay was prepared by lysing frozen saponin-treated parasite pellets in 50 mM HEPES pH 8.0, 150 mM NaCl, 10 mM EDTA pH 8.0, 10% (v/v) glycerol, 1% DDM, followed by centrifugation to obtain soluble lysate. Antibody or nanobody-Fc was added to a final concentration of 1.3 μM to 15 μL of parasite lysate in a 50 μL reaction volume with assay buffer (50 mM HEPES pH 8.0, 150 mM NaCl, 3% (v/v) glycerol, 0.02% DDM), and Input samples were taken. Input and Unbound samples were comprised of 5 μL sample and 5 μL of 2x SDS-PAGE non-reducing sample buffer. 10 μL of a 50% slurry of StrepTactin XT resin (IBA Lifesciences) in assay buffer was added and incubated for 2 h on rollers at 4°C. Samples were centrifuged at 1500 *x* g for 2 min to pellet the resin, and Unbound samples were taken. The resin was washed three times in assay buffer by centrifugation at 1500 *x* g for 2 min. Proteins were eluted from the resin by boiling for 5 min in 15 μL of 2x SDS-PAGE non-reducing sample buffer, followed by centrifugation at 1500 *x* g for 2 min, and 10 μL was taken for the Eluate sample. 10 μL each of Input, Unbound and Eluate samples were run on 3-8% NuPAGE Tris-Acetate gels (ThermoFisher Scientific) in 1X NuPAGE Tris-Acetate running buffer at 150 V for 60 min, then transferred onto a PVDF membrane. All antibody incubations were performed for 1 h at RT, followed by three washes with PBS 0.1% (v/v) Tween-20 at RT for 5 min. The blot was blocked with 10% (v/v) milk in PBS 0.1% Tween-20 overnight at 4°C, then washed and incubated with 2 μg/mL of anti-Pfs48/45 mouse monoclonal antibody 3E12 (*20*, *29*). After washing, the blot was

incubated with HRP-conjugated goat anti-mouse antibody (MerckMillipore AP124P, 1:1000). Finally, the blot was incubated with HRP-conjugated NWSHPQFEK rabbit polyclonal antibody (ThermoFisher Scientific A00875-40, 1:1000). After a final wash with PBS for 10 min, bands were detected using SuperSignal West Pico PLUS Chemiluminescent Substrate (ThermoFisher Scientific) and imaged using a ChemiDoc Imaging System (Bio-Rad).

Crystallization and structure determination of Pfs230 D13D14-nanobody complexes

For crystallization, stable complexes were formed between Pfs230 D13D14 and monomeric nanobodies by mixing antigen and nanobody at a molar ratio of 1:1.5 and incubating for 1 h on ice. Pfs230-nanobody complexes were purified from excess nanobody using SEC in 20 mM HEPES pH 7.5, 150 mM NaCl. Sitting drop vapor diffusion crystallization trials were performed with 5 and 12 mg/mL of complex. Initial crystals of Pfs230 D13D14-W2809 grew in 10% polyethylene glycol (PEG) 8000, 0.2 M sodium acetate, 0.1 M imidazole pH 8.0 at 20ºC and were optimized using hanging drop vapor diffusion by increasing the PEG concentration to 12% as well as incorporating low percentages of cryoprotectant (4% glycerol) within the mother liquor. Crystals of Pfs230 D13D14-W2812 grew in 5% PEG 8000, 5% PEG 10000, 5% PEG 6000, 0.15M ammonium acetate, 0.1 M sodium citrate pH 5.0 at 4 ºC and Pfs230 D13D14-W2810 crystals in 1.4 M sodium malonate dibasic monohydrate pH 7.0 at 20 ºC. For cryo-protection, a premix of 30% PEG 8000 and 10% glycerol within the mother liquor was used for Pfs230 D13D14-W2809 crystals, 30% glycerol in mother liquor was used for Pfs230 D13D14-W2812 and 30% ethylene glycol in mother liquor for Pfs230 D13D14-W2810 crystals, respectively.

Data sets were collected from single crystals on the MX2 beamline at the Australian Synchrotron and processed using the XDS package (*77*). Phaser (*78*) in the CCP4 suite (*79*) was used for molecular replacement using coordinates of a known nanobody structure (PDB ID 8AOK) and an AlphaFold2 (v.2.3.2) predicted model for Pfs230 D13D14 as search models. Structure

refinement was undertaken through iterative rounds of model building in Coot and refinement in Phenix. Figures were prepared in ChimeraX (*56*). Interfaces and interactions were analyzed and buried surface areas calculated using PISA (*80*). The three structures have been deposited in the PDB under accession codes 9E7N (Pfs230 D13D14-W2809), 9E7O (Pfs230 D13D14-W2810) and 9E7P (Pfs230 D13D14-W2812).

Standard membrane feeding assays

Standard membrane feeding assays were conducted at Seattle Children's Research Institute using the *P. falciparum* NF54 line (*81*). To initiate gametocyte development, healthy asexual cultures, primarily containing ring-stage parasites, were set up at 1% parasitemia and 5% hematocrit in a 6-well plate. Gametocyte cultures were maintained for 14 days, with daily media changes. On day 15, stage V gametocytes were evaluated, and female *Anopheles stephensi* mosquitoes (4-7 days old) were fed on mature gametocyte cultures at 0.3% gametocytemia and 50% hematocrit. Nanobody-Fcs were added to the blood meal at a final concentration of 100–200 µg/mL. LMIV230-01, used as a positive control, was included at a concentration of 200 µg/mL. After one week, midguts were dissected, and oocyst numbers were enumerated. Standard membrane feeding assays for the 230ΔD1314 lines were conducted at WEHI using a similar approach as above without the addition of nanobodies. Assays performed using pooled mouse pre-immune and 230D13D14S and 230D13D14L mRNA-LNP sera were conducted at WEHI using a similar approach as above with pooled mouse serum added at a final concentration of 1:5.

Papua New Guinea (PNG) study populations

Plasma samples were obtained from children (aged 5-10 years) in PNG that participated in a randomized double-blind drug trial (*82*). For this experiment, the final time point of the sample collection at 36 weeks post-enrolment was used. Thirty-two samples were selected from children

who were currently infected with *P. falciparum* at this timepoint; of these, 13 were co-infected with *P. vivax*. Forty samples were included from PNG children who did not have a current *Plasmodium* infection at the time of sample collection, but live in the same endemic area, with 27.5% having had PCR-detectable *P. falciparum* infections during the prior 36-week period (47.5% had PCR-detectable *P. vivax* infections). These children were randomly selected and had equivalent demographics to the 32 *P. falciparum* positive children. Forty negative control samples were selected from the Volunteer Biospecimen Donor Registry (VBDR) in Melbourne. The studies involving human participants were reviewed and approved by the Walter and Eliza Hall Institute Human Research Ethics Committee (13/07), the PNG Institute of Medical Research Institutional Review Board (0908) and the PNG Medical Advisory Committee (09.11). All individuals gave informed consent and/or assent to participate in the study.

Antigen coupling to magnetic beads

Five different protein constructs of Pfs230 and Pvs230 were included in the Luminex antibody detection assay. Of these, four were from different 6-cysteine domains of Pfs230, namely D1D2, D5D6, D11D12, and D13D14, and the other was from D13 and D14 of Pvs230, assigned as PvD13D14. These constructs were coupled to magnetic Bio-Plex beads (Bio-Rad) following the manufacturer's instructions and as per prior publications (*43*). Briefly, the protein constructs were coupled to uniquely fluorescent microspheres. 50 µL of each microsphere was taken from the stock into a 1.5 mL tube after sonication and vortexing for 15 s and 10 s, respectively. The tubes were immobilized in a magnetic separator rack for 30 – 60 s. The supernatant was discarded, and the remaining microspheres washed with 100 µL of MilliQ water. The suspension was vortexed for 20 s and the supernatant was discarded. The COOH functional group of the microspheres were activated with the addition of 80 µL of monobasic sodium phosphate (100 mM, pH 6.2), 10 µL of sulfo-N-hydrosuccinimide (50 mg/mL) and 10 µL of N-ethyl-N-(3-

dimethylaminopropyl) cabodiimide (EDC) (50 mg/mL). The mixture was incubated for 20 min in the dark at RT on a rotator. The microspheres were washed twice with 500 µL of 1X PBS (pH 7.4) and vortexed for 20 s. The activated microspheres were resuspended with 248 µL of 1X PBS, followed by the addition of 2 µg of the antigen. The mixture was then incubated at RT for 2 h on the rotator. Afterwards, the mixture was washed three times with 500 µL of 1X PBS-TBN (PBS, 0.1% (w/v) bovine serum albumin (BSA), 0.02% (v/v) TWEEN-20, 0.05% azide, pH 7) and then resuspended in 125 µL of 1X PBS-TBN. The mixture was kept at 4 °C in the dark until use.

Multiplex antibody assay

Plasma samples were diluted in PBT (1X PBS, 1% BSA, 0.05% Tween-20) at a dilution of 1:100. Plasma samples from hyper-immune individuals from PNG were used as a positive control pool from which a two-fold serial dilution curve was derived, as previously described (*43*). Plasma samples from malaria-naïve individuals from the VBDR were used as the negative control pool. 50 µL of the 1:100 diluted sample was added to a black flat-bottom 96-well plate. A bead mixture with all the coupled microspheres was prepared and 50 µL of this mixture was added to the plate, which was then incubated for 30 min in the dark on a plate shaker. The plate was washed three times with PBST (1X PBS, 0.05% TWEEN-20) using a plate washer. 100 µL of phycoerythrin (PE)-conjugated anti-human secondary antibody (Jackson Immunoresearch) at 1:100 dilution was added to each well and the plate was incubated for 15 min. After a wash, the wells were resuspended with 100 µL PBT and incubated for 5 min on a plate shaker before the plate was read on the MAGPIX instrument. Median fluorescence intensity was obtained and converted to relative antibody units using the PNG serial dilution curve on each plate. This conversion is performed using a five-parameter logistic regression model (*43*).

Production of mRNA-LNP vaccines

mRNA production

The mRNAs used in this study were produced using HiScribe T7 mRNA synthesis kit (NEB, Australia) using linearized DNA produced by PCR amplification. The transcribed mRNAs included a 3'-UTR with Kozak sequence, 5'-UTR and polyA$_{125}$ tails. The codon sequences were optimized to reduce the uridine content of mRNA. We used N1-methyl-pseudoUTP instead of UTP to produce chemically modified mRNA, in common with the two approved COVID-19 vaccines. CleanCap reagent AG (TriLink) was used in accordance with the manufacturer's recommendations to produce Cap1 chemistry at the 5' terminus. The mRNA was subject to cellulose purification before use.

Lipid nanoparticle (LNP) formulation

The following lipids were used in the study: ionisable lipid [(4-hydroxybutyl)-azanediyl]-di-(hexane-6,1-diyl)-bis-(2-hexyldecanoate) (ALC-0315), cholesterol (Sigma-Aldrich, Germany), 1,2-distearoyl-sn-glycero-3-phosphocholine (DSPC) (Avanti Polar Lipids Inc., USA), and the PEGylated lipid methoxypolyethyleneglycoloxy(2000)-N,N-ditetradecylacetamide (ALC-0159). The lipids were used in the proportions used in the BioNTech/Pfizer SARS-CoV-2 mRNA vaccine (*Comirnaty*). Formulations of the vaccines into LNPs involved the following steps: an aqueous solution of mRNA at pH4 was mixed with a solution of the four lipids in ethanol, using a microfluidics mixing device (NxGen Ignite Nanoassemblr) supplied by Precision Nanosystems. The suspension of nanoparticles was adjusted to pH of 7.4 using a 1:3 dilution in Tris buffer, then dialyzed against 25 mM Tris buffer to remove the ethanol. The LNP suspension was adjusted with sucrose solution to produce the cryoprotected, isotonic final form of the product. The product was sterile filtered (0.22 μm) prior to being aliquoted into sterile vials for storage at -80°C. Characterization of the LNPs included analysis for RNA content, encapsulation efficiency and RNA integrity. Particle size and polydispersity index (PDI) were determined by dynamic light scattering, a standard method for submicron dispersions, using a Zetasizer (Malvern Instruments).

Typically, encapsulation efficiency was 85-95%, particle sizes (Z-average) of the LNPs were 78 – 81 nm after thawing with PDI < 0.2. All the procedures were carried out by mRNA Core (mrnacore.org).

Pfs230 D13D14 mRNA-LNPs immunization

Mouse immunization and serum isolation were performed by the WEHI Antibody Facility. Groups of 8–12 week old female C57BL/6 mice (n=6) were immunized with 10 µg of either 230D13D14L or 230D13D14S mRNA-LNP alone. The mRNA-LNPs were administered intramuscularly in a 50 µL dose per mouse. Mice were immunized on day 1 and day 28. For pre-immune sera, mice were bled on day 1 prior to immunization. Mice were also bled on day 21 and day 68 for the first and second bleed, respectively. This work has been approved by the WEHI Animal Ethics Committee 2023.012.

ELISA for antibody levels

96-well flat-bottomed MaxiSorp plates were coated with 50 µL of 1 µg/mL recombinant Pfs230 D13D14 in 1x PBS for 1 h at RT. All washes were done three times using PBST and all incubations were performed for 1 h at RT. Coated plates were washed and blocked with 1% BSA in PBST for 1 h. Plates were washed and incubated with two-fold serial dilutions of mouse sera starting at 1:200 in 1% BSA PBST, washed as above and incubated with horseradish peroxidase (HRP)-conjugated goat anti-mouse secondary antibody (1:2000; Merck AP124P). 50 µL of ABTS liquid substrate (Sigma 11684302001) was added and incubated at RT and 50 µL of 1% SDS was used to stop the reaction. Absorbance was read at OD 405 nm and all samples were in duplicate. The serial dilution curves were fitted to a third order polynomial regression curve using GraphPad Prism version 10 for Mac (GraphPad Software). End point titers were determined as the reciprocal of the dilution at which the curve intersected the cutoff, and the cutoff was defined as three times the average absorbance values of the respective pre-immune serum.

Quantification and statistical analysis

Analyses were performed using GraphPad Prism version 10 for Mac (GraphPad Software). Tests and statistics are described in Figure Legends. For end point titers, the serial dilution curves were fitted to a third order polynomial regression curve using GraphPad Prism version 10 for Mac (GraphPad Software). End point titers were determined as the reciprocal of the dilution at which the curve intersected the cutoff, and the cutoff was defined as three times the average absorbance values of the respective pre-immune serum. Automated quantitation of SIFA of macrogametes were performed as follows. Cell segmentation was performed via a custom trained cellpose (*66*, *67*) network on maximum intensity projected brightfield images. Cell scoring was performed via a custom FIJI (*64*) macro with manual thresholds set for mean intensity of maximum intensity projected images of 647 and 555 channels. Mask images showing the segmentation and scoring of each cell were produced for manual validation.

References and notes

1. WHO, "World Malaria Report 2024" (2024).
2. R. E. Sinden, Developing transmission-blocking strategies for malaria control. *PLoS Pathog.* **13**, e1006336 (2017).
3. S. A. Arredondo, M. Cai, Y. Takayama, N. J. MacDonald, D. E. Anderson, L. Aravind, G. M. Clore, L. H. Miller, Structure of the Plasmodium 6-cysteine s48/45 domain. *Proc. Natl. Acad. Sci. U.S.A.* **109**, 6692–7 (2012).
4. F. M. T. Lyons, M. Gabriela, W.-H. Tham, M. H. Dietrich, Plasmodium 6-Cysteine Proteins: Functional Diversity, Transmission-Blocking Antibodies and Structural Scaffolds. *Front. Cell. Infect. Microbiol.* **12**, 945924 (2022).
5. N. Kumar, Target antigens of malaria transmission blocking immunity exist as a stable membrane bound complex. *Parasite Immunol.* **9**, 321–335 (1987).
6. N. Kumar, B. Wizel, Further characterization of interactions between gamete surface antigens of Plasmodium falciparum. *Mol. Biochem. Parasitol.* **53**, 113–120 (1992).

7. T. J. Templeton, D. C. Kaslow, Identification of additional members define a Plasmodium falciparum gene superfamily which includes Pfs48/45 and Pfs230. *Mol. Biochem. Parasitol.* **101**, 223–227 (1999).

8. C. H. M. Kocken, J. Jansen, A. M. Kaan, P. J. A. Beckers, T. Ponnudurai, D. C. Kaslow, R. N. H. Konings, J. G. G. Schoenmakers, Cloning and expression of the gene coding for the transmission blocking target antigen Pfs48/45 of Plasmodium falciparum. *Mol. Biochem. Parasitol.* **61**, 59–68 (1993).

9. A. N. Vermeulen, T. Ponnudurai, P. J. A. Beckers, JP. Verhave, M. A. Smits, J. H. E. T. Meuwissen, Sequential expression of antigens on sexual stages of Plasmodium falciparum accessible to transmission-blocking antibodies in the mosquito. *J. Exp. Med.* **162**, 1460–1476 (1985).

10. M. R. van Dijk, B. C. van Schaijk, S. M. Khan, M. W. van Dooren, J. Ramesar, S. Kaczanowski, G. J. van Gemert, H. Kroeze, H. G. Stunnenberg, W. M. Eling, R. W. Sauerwein, A. P. Waters, C. J. Janse, Three members of the 6-cys protein family of Plasmodium play a role in gamete fertility. *PLoS Pathog.* **6**, e1000853 (2010).

11. J. Rener, P. M. Graves, R. Carter, J. L. Williams, T. R. Burkot, Target antigens of transmission-blocking immunity on gametes of plasmodium falciparum. *J. Exp. Med.* **158**, 976–981 (1983).

12. S. Eksi, B. Czesny, G. J. van Gemert, R. W. Sauerwein, W. Eling, K. C. Williamson, Malaria transmission-blocking antigen, Pfs230, mediates human red blood cell binding to exflagellating male parasites and oocyst production. *Mol. Microbiol.* **61**, 991–8 (2006).

13. R. S. Ramiro, S. M. Khan, B. Franke-Fayard, C. J. Janse, D. J. Obbard, S. E. Reece, Hybridization and pre-zygotic reproductive barriers in Plasmodium. *Proc. R. Soc. B.* **282**, 20143027 (2015).

14. M. R. van Dijk, C. J. Janse, J. Thompson, A. P. Waters, J. A. M. Braks, H. J. Dodemont, H. G. Stunnenberg, G. J. van Gemert, R. Sauerwein, W. Eling, A Central Role for P48/45 in Malaria Parasite Male Gamete Fertility. *Cell* **104**, 153–164 (2001).

15. M. Tachibana, Y. Wu, H. Iriko, O. Muratova, N. J. MacDonald, J. Sattabongkot, S. Takeo, H. Otsuki, M. Torii, T. Tsuboi, N-terminal prodomain of Pfs230 synthesized using a cell-free system is sufficient to induce complement-dependent malaria transmission-blocking activity. *Clin. Vaccine Immunol.* **18**, 1343–50 (2011).

16. M. Tachibana, K. Miura, E. Takashima, M. Morita, H. Nagaoka, L. Zhou, C. A. Long, C. Richter King, M. Torii, T. Tsuboi, T. Ishino, Identification of domains within Pfs230 that elicit transmission blocking antibody responses. *Vaccine* **37**, 1799–1806 (2019).

17. K. C. Williamson, D. B. Keister, O. Muratova, D. C. Kaslow, Recombinant Pfs230, a Plasmodium falciparum gametocyte protein, induces antisera that reduce the infectivity of Plasmodium falciparum to mosquitoes. *Mol. Biochem. Parasitol.* **75**, 33–42 (1995).

18. K. Miura, E. Takashima, T. P. Pham, B. Deng, L. Zhou, W. C. Huang, A. Diouf, Y. T. Gebremicale, M. Tachibana, T. Ishino, C. Richter King, J. F. Lovell, C. A. Long, T. Tsuboi, Elucidating functional epitopes within the N-terminal region of malaria transmission blocking vaccine antigen Pfs230. *npj Vaccines* **7**, 4 (2022).

19. C. H. Coelho, W. K. Tang, M. Burkhardt, J. D. Galson, O. Muratova, N. D. Salinas, E. S. T. L. Alves, K. Reiter, N. J. MacDonald, V. Nguyen, R. Herrera, R. Shimp, D. L. Narum, M. Byrne-Steele, W. Pan, X. Hou, B. Brown, M. Eisenhower, J. Han, B. J. Jenkins, J. Y. A. Doritchamou, M. G. Smelkinson, J. Vega-Rodriguez, J. Truck, J. J. Taylor, I. Sagara, J. P. Renn, N. H. Tolia, P. E. Duffy, A human monoclonal antibody blocks malaria transmission and defines a highly conserved neutralizing epitope on gametes. *Nat. Commun.* **12**, 1750 (2021).

20. K. Singh, M. Burkhardt, S. Nakuchima, R. Herrera, O. Muratova, A. G. Gittis, E. Kelnhofer, K. Reiter, M. Smelkinson, D. Veltri, B. J. Swihart, R. Shimp Jr., V. Nguyen, B. Zhang, N. J. MacDonald, P. E. Duffy, D. N. Garboczi, D. L. Narum, Structure and function of a malaria transmission blocking vaccine targeting Pfs230 and Pfs230-Pfs48/45 proteins. *Commun. Biol.* **3**, 395 (2020).

21. J. Plieskatt, E. A. Ofori, M. Naghizadeh, K. Miura, Y. Flores-Garcia, N. Borbye-Lorenzen, A. B. Tiono, K. Skogstrand, I. Sagara, F. Zavala, M. Theisen, ProC6C, a novel multi-stage malaria vaccine, elicits functional antibodies against the minor and central repeats of the Circumsporozoite Protein in human adults. *Front. Immunol.* **15**, 1481829 (2024).

22. S. A. Healy, C. Anderson, B. J. Swihart, A. Mwakingwe, E. E. Gabriel, H. Decederfelt, C. V. Hobbs, K. M. Rausch, D. Zhu, O. Muratova, R. Herrera, P. V. Scaria, N. J. MacDonald, L. E. Lambert, I. Zaidi, C. H. Coelho, J. P. Renn, Y. Wu, D. L. Narum, P. E. Duffy, Pfs230 yields higher malaria transmission-blocking vaccine activity than Pfs25 in humans but not mice. *J. Clin. Invest.* **131**, e146221 (2021).

23. N. D. Salinas, R. Ma, T. H. Dickey, H. McAleese, T. Ouahes, C. A. Long, K. Miura, L. E. Lambert, N. H. Tolia, A potent and durable malaria transmission-blocking vaccine designed from a single-component 60-copy Pfs230D1 nanoparticle. *npj Vaccines* **8**, 124 (2023).

24. N. D. Salinas, R. Ma, H. McAleese, T. Ouahes, C. A. Long, K. Miura, L. E. Lambert, N. H. Tolia, A Self-Assembling Pfs230D1-Ferritin Nanoparticle Vaccine Has Potent and Durable Malaria Transmission-Reducing Activity. *Vaccines* **12**, 546 (2024).

25. M. H. Dietrich, M. Gabriela, K. Reaksudsan, M. W. A. Dixon, L. J. Chan, A. Adair, S. Trickey, M. T. O'Neill, L. L. Tan, S. Lopaticki, J. Healer, S. Keremane, A. Cowman, W. H. Tham, Nanobodies against Pfs230 block Plasmodium falciparum transmission. *Biochem. J.* **479**, 2529–2546 (2022).

26. D. Ivanochko, A. Fabra-García, K. Teelen, M. van de Vegte-Bolmer, G.-J. van Gemert, J. Newton, A. Semesi, M. de Bruijni, J. Bolscher, J. Ramjith, M. Szabat, S. Vogt, L. Kraft, S. Duncan, S.-M. Lee, M. R. Kamya, M. E. Feeney, P. Jagannathan, B. Greenhouse, R. W. Sauerwein, C. Richter King, R. S. MacGill, T. Bousema, M. M. Jore, J.-P. Julien, Potent transmission-blocking monoclonal antibodies from naturally exposed individuals target a conserved epitope on Plasmodium falciparum Pfs230. *Immunity* **56**, 420-432.e7 (2023).

27. W. K. Tang, C. H. Coelho, K. Miura, B. C. Nguemwo Tentokam, N. D. Salinas, D. L. Narum, S. A. Healy, I. Sagara, C. A. Long, P. E. Duffy, N. H. Tolia, A human antibody epitope map of Pfs230D1 derived from analysis of individuals vaccinated with a malaria transmission-blocking vaccine. *Immunity* **56**, 433-443.e5 (2023).

28. K. T. Ko, F. Lennartz, D. Mekhaiel, B. Guloglu, A. Marini, D. J. Deuker, C. A. Long, M. M. Jore, K. Miura, S. Biswas, M. K. Higgins, Structure of the malaria vaccine candidate Pfs48/45 and its recognition by transmission blocking antibodies. *Nat. Commun.* **13**, 5603 (2022).

29. R. Carter, P. M. Graves, D. B. Keister, I. A. Quakyi, Properties of epitopes of Pfs 48/45, a target of transmission blocking monoclonal antibodies, on gametes of different isolates of Plasmodium falciparum. *Parasite Immunol.* **12**, 587–603 (1990).

30. N. Outchkourov, A. Vermunt, J. Jansen, A. Kaan, W. Roeffen, K. Teelen, E. Lasonder, A. Braks, M. van de Vegte-Bolmer, L. Y. Qiu, R. Sauerwein, H. G. Stunnenberg, Epitope analysis of the malaria surface antigen pfs48/45 identifies a subdomain that elicits transmission blocking antibodies. *J. Biol. Chem.* **282**, 17148–56 (2007).

31. A. Fabra-Garcia, S. Hailemariam, R. M. de Jong, K. Janssen, K. Teelen, M. van de Vegte-Bolmer, G. J. van Gemert, D. Ivanochko, A. Semesi, B. McLeod, M. W. Vos, M. H. C. de Bruijni, J. M. Bolscher, M. Szabat, S. Vogt, L. Kraft, S. Duncan, M. R. Kamya, M. E. Feeney, P. Jagannathan, B. Greenhouse, K. J. Dechering, R. W. Sauerwein, C. R. King, R. S. MacGill, T. Bousema, J. P. Julien, M. M. Jore, Highly potent, naturally acquired human monoclonal antibodies against Pfs48/45 block Plasmodium falciparum transmission to mosquitoes. *Immunity* **56**, 406-419.e7 (2023).

32. L. M. Simons, P. Ferrer, N. Gombakomba, K. Underwood, R. Herrera, D. L. Narum, G. Canepa, F. Acquah, L. Amoah, P. E. Duffy, C. Barillas-Mury, C. Long, S. M. Lee, E. Locke, K. Miura, K. C. Williamson, Extending the range of Plasmodium falciparum transmission blocking antibodies. *Vaccine* **41**, 3367–3379 (2023).

33. W. Roeffen, K. Teelen, J. van As, M. vd Vegte-Bolmer, W. Eling, R. Sauerwein, Plasmodium falciparum: production and characterization of rat monoclonal antibodies specific for the sexual-stage Pfs48/45 antigen. *Exp. Parasitol.* **97**, 45–9 (2001).

34. R. Carter, A. Coulson, S. Bhatti, B. J. Taylor, J. F. Elliott, Predicted disulfide-bonded structures for three uniquely related proteins of Plasmodium falciparum, Pfs230, Pfs48/45 and Pf12. *Mol. Biochem. Parasitol.* **71**, 203–210 (1995).

35. D. L. Gerloff, A. Creasey, S. Maslau, R. Carter, Structural models for the protein family characterized by gamete surface protein Pfs230 of Plasmodium falciparum. *Proc. Natl. Acad. Sci. U.S.A.* **102**, 13598–603 (2005).

36. M. L. Parker, F. Peng, M. J. Boulanger, The Structure of Plasmodium falciparum Blood-Stage 6-Cys Protein Pf41 Reveals an Unexpected Intra-Domain Insertion Required for Pf12 Coordination. *PLoS ONE* **10**, e0139407 (2015).

37. M. L. Tonkin, S. A. Arredondo, B. C. Loveless, J. J. Serpa, K. A. Makepeace, N. Sundar, E. V. Petrotchenko, L. H. Miller, M. E. Grigg, M. J. Boulanger, Structural and biochemical

characterization of Plasmodium falciparum 12 (Pf12) reveals a unique interdomain organization and the potential for an antiparallel arrangement with Pf41. *J. Biol. Chem.* **288**, 12805–17 (2013).

38. M. H. Dietrich, L. J. Chan, A. Adair, S. Keremane, P. Pymm, A. W. Lo, Y. C. Cao, W. H. Tham, Nanobody generation and structural characterization of Plasmodium falciparum 6-cysteine protein Pf12p. *Biochem. J.* **478**, 579–595 (2021).

39. M. H. Dietrich, L. J. Chan, A. Adair, C. Boulet, M. T. O'Neill, L. L. Tan, S. Keremane, Y. F. Mok, A. W. Lo, P. Gilson, W. H. Tham, Structure of the Pf12 and Pf41 heterodimeric complex of Plasmodium falciparum 6-cysteine proteins. *FEMS Microbes* **3**, xtac005 (2022).

40. P. Kundu, A. Semesi, M. M. Jore, M. J. Morin, V. L. Price, A. Liang, J. Li, K. Miura, R. W. Sauerwein, C. R. King, J. P. Julien, Structural delineation of potent transmission-blocking epitope I on malaria antigen Pfs48/45. *Nat. Commun.* **9**, 4458 (2018).

41. S. D. Boltryk, A. Passecker, A. Alder, E. Carrington, M. van de Vegte-Bolmer, G. J. van Gemert, A. van der Starre, H. P. Beck, R. W. Sauerwein, T. W. A. Kooij, N. M. B. Brancucci, N. I. Proellochs, T. W. Gilberger, T. S. Voss, CRISPR/Cas9-engineered inducible gametocyte producer lines as a valuable tool for Plasmodium falciparum malaria transmission research. *Nat. Commun.* **12**, 4806 (2021).

42. P. Pymm, A. Adair, L. J. Chan, J. P. Cooney, F. L. Mordant, C. C. Allison, E. Lopez, E. R. Haycroft, M. T. O'Neill, L. L. Tan, M. H. Dietrich, D. Drew, M. Doerflinger, M. A. Dengler, N. E. Scott, A. K. Wheatley, N. A. Gherardin, H. Venugopal, D. Cromer, M. P. Davenport, R. Pickering, D. I. Godfrey, D. F. J. Purcell, S. J. Kent, A. W. Chung, K. Subbarao, M. Pellegrini, A. Glukhova, W. H. Tham, Nanobody cocktails potently neutralize SARS-CoV-2 D614G N501Y variant and protect mice. *Proc. Natl. Acad. Sci. U.S.A.* **118**, e2101918118 (2021).

43. R. Mazhari, J. Brewster, R. Fong, C. Bourke, Z. S. J. Liu, E. Takashima, T. Tsuboi, W.-H. Tham, M. Harbers, C. Chitnis, J. Healer, M. Ome-Kaius, J. Sattabongkot, J. Kazura, L. J. Robinson, C. King, I. Mueller, R. J. Longley, A comparison of non-magnetic and magnetic beads for measuring IgG antibodies against Plasmodium vivax antigens in a multiplexed bead-based assay using Luminex technology (Bio-Plex 200 or MAGPIX). *PLoS ONE* **15**, e0238010 (2020).

44. A. Quakyi, R. Carter, J. Rener, N. Kumar, M. F. Good, L. H. Miller, The 230-kDa gamete surface protein of Plasmodium falciparum is also a target for transmission-blocking antibodies. *J. Immunol.* **139**, 4213–4217 (1987).

45. N. J. MacDonald, V. Nguyen, R. Shimp, K. Reiter, R. Herrera, M. Burkhardt, O. Muratova, K. Kumar, J. Aebig, K. Rausch, L. Lambert, N. Dawson, J. Sattabongkot, X. Ambroggio, P. E. Duffy, Y. Wu, D. L. Narum, Structural and Immunological Characterization of Recombinant 6-Cysteine Domains of the Plasmodium falciparum Sexual Stage Protein Pfs230. *J. Biol. Chem.* **291**, 19913–22 (2016).

46. M. R. Inklaar, R. M. de Jong, E. T. Bekkering, H. Nagaoka, F. L. Fennemann, K. Teelen, M. van de Vegte-Bolmer, G.-J. van Gemert, R. Stoter, C. R. King, N. I. Proellochs, T. Bousema,

E. Takashima, T. Tsuboi, M. M. Jore, Pfs230 Domain 7 is targeted by a potent malaria transmission-blocking monoclonal antibody. *npj Vaccines* **8**, 186 (2023).

47. W. Roeffen, F. Geeraedts, W. Eling, P. Beckers, B. Wizel, N. Kumar, T. Lensen, R. Sauerwein, Transmission blockade of Plasmodium falciparum malaria by anti-Pfs230-specific antibodies is isotype dependent. *Infect. Immun.* **63**, 467–471 (1995).

48. W. Roeffen, P. J. A. Beckers, T. K. Lensen, R. W. Sauerwein, J. H. E. T. Meuwissen, W. Eling, Plasmodium falciparum: A Comparison of the Activity of Pfs230-Specific Antibodies in an Assay of Transmission-Blocking Immunity and Specific Competition ELISAs. *Exp. Parasitol.* **80**, 15–26 (1995).

49. P. V. Scaria, N. Roth, K. Schwendt, O. V. Muratova, N. Alani, L. E. Lambert, E. K. Barnafo, C. G. Rowe, I. U. Zaidi, K. M. Rausch, D. L. Narum, B. Petsch, P. E. Duffy, mRNA vaccines expressing malaria transmission-blocking antigens Pfs25 and Pfs230D1 induce a functional immune response. *npj Vaccines* **9**, 9 (2024).

50. M. Ghorbal, M. Gorman, C. R. Macpherson, R. M. Martins, A. Scherf, J. J. Lopez-Rubio, Genome editing in the human malaria parasite Plasmodium falciparum using the CRISPR-Cas9 system. *Nat. Biotechnol.* **32**, 819–21 (2014).

51. R. W. Moon, J. Hall, F. Rangkuti, Y. S. Ho, N. Almond, G. H. Mitchell, A. Pain, A. A. Holder, M. J. Blackman, Adaptation of the genetically tractable malaria pathogen Plasmodium knowlesi to continuous culture in human erythrocytes. *Proc. Natl. Acad. Sci. U.S.A.* **110**, 531–536 (2013).

52. A. Punjani, J. L. Rubinstein, D. J. Fleet, M. A. Brubaker, cryoSPARC: algorithms for rapid unsupervised cryo-EM structure determination. *Nat. Methods* **14**, 290–296 (2017).

53. J. He, T. Li, S.-Y. Huang, Improvement of cryo-EM maps by simultaneous local and non-local deep learning. *Nat. Commun.* **14**, 3217 (2023).

54. J. Jumper, R. Evans, A. Pritzel, T. Green, M. Figurnov, O. Ronneberger, K. Tunyasuvunakool, R. Bates, A. Zidek, A. Potapenko, A. Bridgland, C. Meyer, S. A. A. Kohl, A. J. Ballard, A. Cowie, B. Romera-Paredes, S. Nikolov, R. Jain, J. Adler, T. Back, S. Petersen, D. Reiman, E. Clancy, M. Zielinski, M. Steinegger, M. Pacholska, T. Berghammer, S. Bodenstein, D. Silver, O. Vinyals, A. W. Senior, K. Kavukcuoglu, P. Kohli, D. Hassabis, Highly accurate protein structure prediction with AlphaFold. *Nature* **596**, 583–589 (2021).

55. R. Evans, M. O'Neill, A. Pritzel, N. Antropova, A. Senior, T. Green, A. Žídek, R. Bates, S. Blackwell, J. Yim, O. Ronneberger, S. Bodenstein, M. Zielinski, A. Bridgland, A. Potapenko, A. Cowie, K. Tunyasuvunakool, R. Jain, E. Clancy, P. Kohli, J. Jumper, D. Hassabis, Protein complex prediction with AlphaFold-Multimer. *bioRxiv*, doi: 10.1101/2021.10.04.463034 (2022).

56. T. D. Goddard, C. C. Huang, E. C. Meng, E. F. Pettersen, G. S. Couch, J. H. Morris, T. E. Ferrin, UCSF ChimeraX: Meeting modern challenges in visualization and analysis. *Protein Sci.* **27**, 14–25 (2018).

57. R. T. Kidmose, J. Juhl, P. Nissen, T. Boesen, J. L. Karlsen, B. P. Pedersen, Namdinator – automatic molecular dynamics flexible fitting of structural models into cryo-EM and crystallography experimental maps. *IUCrJ* **6**, 526–531 (2019).

58. D. Liebschner, P. V. Afonine, M. L. Baker, G. Bunkoczi, V. B. Chen, T. I. Croll, B. Hintze, L. W. Hung, S. Jain, A. J. McCoy, N. W. Moriarty, R. D. Oeffner, B. K. Poon, M. G. Prisant, R. J. Read, J. S. Richardson, D. C. Richardson, M. D. Sammito, O. V. Sobolev, D. H. Stockwell, T. C. Terwilliger, A. G. Urzhumtsev, L. L. Videau, C. J. Williams, P. D. Adams, Macromolecular structure determination using X-rays, neutrons and electrons: recent developments in Phenix. *Acta Crystallogr D Struct Biol* **75**, 861–877 (2019).

59. P. Emsley, B. Lohkamp, W. G. Scott, K. Cowtan, Features and development of ıt Coot. *Acta Cryst.* **D66**, 486–501 (2010).

60. L.-Y. Liang, M. Roy, C. R. Horne, J. J. Sandow, M. Surudoi, L. F. Dagley, S. N. Young, T. Dite, J. J. Babon, P. W. Janes, O. Patel, J. M. Murphy, I. S. Lucet, The intracellular domains of the EphB6 and EphA10 receptor tyrosine pseudokinases function as dynamic signalling hubs. *Biochem. J.* **478**, 3351–3371 (2021).

61. M. C. Chambers, B. Maclean, R. Burke, D. Amodei, D. L. Ruderman, S. Neumann, L. Gatto, B. Fischer, B. Pratt, J. Egertson, K. Hoff, D. Kessner, N. Tasman, N. Shulman, B. Frewen, T. A. Baker, M.-Y. Brusniak, C. Paulse, D. Creasy, L. Flashner, K. Kani, C. Moulding, S. L. Seymour, L. M. Nuwaysir, B. Lefebvre, F. Kuhlmann, J. Roark, P. Rainer, S. Detlev, T. Hemenway, A. Huhmer, J. Langridge, B. Connolly, T. Chadick, K. Holly, J. Eckels, E. W. Deutsch, R. L. Moritz, J. E. Katz, D. B. Agus, M. MacCoss, D. L. Tabb, P. Mallick, A cross-platform toolkit for mass spectrometry and proteomics. *Nat. Biotechnol.* **30**, 918–920 (2012).

62. M. L. Mendes, L. Fischer, Z. A. Chen, M. Barbon, F. J. O'Reilly, S. H. Giese, M. Bohlke-Schneider, A. Belsom, T. Dau, C. W. Combe, M. Graham, M. R. Eisele, W. Baumeister, C. Speck, J. Rappsilber, An integrated workflow for crosslinking mass spectrometry. *Mol. Syst. Biol.* **15**, e8994 (2019).

63. C. W. Combe, M. Graham, L. Kolbowski, L. Fischer, J. Rappsilber, xiVIEW: Visualisation of Crosslinking Mass Spectrometry Data. *J. Mol. Biol.* **436**, 168656 (2024).

64. J. Schindelin, I. Arganda-Carreras, E. Frise, V. Kaynig, M. Longair, T. Pietzsch, S. Preibisch, C. Rueden, S. Saalfeld, B. Schmid, J.-Y. Tinevez, D. J. White, V. Hartenstein, K. Eliceiri, P. Tomancak, A. Cardona, Fiji: an open-source platform for biological-image analysis. *Nat. Methods* **9**, 676–682 (2012).

65. M. J. Delves, U. Straschil, A. Ruecker, C. Miguel-Blanco, S. Marques, A. C. Dufour, J. Baum, R. E. Sinden, Routine in vitro culture of P. falciparum gametocytes to evaluate novel transmission-blocking interventions. *Nat. Protoc.* **11**, 1668–80 (2016).

66. C. Stringer, T. Wang, M. Michaelos, M. Pachitariu, Cellpose: a generalist algorithm for cellular segmentation. *Nat. Methods* **18**, 100–106 (2021).

67. M. Pachitariu, C. Stringer, Cellpose 2.0: how to train your own model. *Nat. Methods* **19**, 1634–1641 (2022).

68. E. Pardon, T. Laeremans, S. Triest, S. G. Rasmussen, A. Wohlkonig, A. Ruf, S. Muyldermans, W. G. Hol, B. K. Kobilka, J. Steyaert, A general protocol for the generation of Nanobodies for structural biology. *Nat. Protoc.* **9**, 674–93 (2014).

69. T. Magoč, S. L. Salzberg, FLASH: fast length adjustment of short reads to improve genome assemblies. *Bioinformatics* **27**, 2957–2963 (2011).

70. J. Ye, N. Ma, T. L. Madden, J. M. Ostell, IgBLAST: an immunoglobulin variable domain sequence analysis tool. *Nucleic Acids Res.* **41**, W34–W40 (2013).

71. M.-P. Lefranc, IMGT, the International ImMunoGeneTics Information System. *Cold Spring Harb. Protoc.* **2011**, 595–603 (2011).

72. N. Saitou, M. Nei, The neighbor-joining method: a new method for reconstructing phylogenetic trees. *Mol. Biol. Evol.* **4**, 406–425 (1987).

73. K. P. Schliep, phangorn: phylogenetic analysis in R. *Bioinformatics* **27**, 592–593 (2011).

74. G. Yu, T. T.-Y. Lam, H. Zhu, Y. Guan, Two Methods for Mapping and Visualizing Associated Data on Phylogeny Using Ggtree. *Mol. Biol. Evol.* **35**, 3041–3043 (2018).

75. R Core Team, R: A language and environment for statistical computing, R Foundation for Statistical Computing (2020); https://www.R-project.org/.

76. O. Wagih, ggseqlogo: a versatile R package for drawing sequence logos. *Bioinformatics* **33**, 3645–3647 (2017).

77. W. Kabsch, Xds. *Acta Crystallogr D Biol Crystallogr* **66**, 125–32 (2010).

78. M. Grayling J., phaseR: An R Package for Phase Plane Analysis of Autonomous ODE Systems. *The R Journal* **6**, 43 (2014).

79. J. Agirre, M. Atanasova, H. Bagdonas, C. B. Ballard, A. Baslé, J. Beilsten-Edmands, R. J. Borges, D. G. Brown, J. J. Burgos-Mármol, J. M. Berrisford, P. S. Bond, I. Caballero, L. Catapano, G. Chojnowski, A. G. Cook, K. D. Cowtan, T. I. Croll, J. É. Debreczeni, N. E. Devenish, E. J. Dodson, T. R. Drevon, P. Emsley, G. Evans, P. R. Evans, M. Fando, J. Foadi, L. Fuentes-Montero, E. F. Garman, M. Gerstel, R. J. Gildea, K. Hatti, M. L. Hekkelman, P. Heuser, S. W. Hoh, M. A. Hough, H. T. Jenkins, E. Jiménez, R. P. Joosten, R. M. Keegan, N. Keep, E. B. Krissinel, P. Kolenko, O. Kovalevskiy, V. S. Lamzin, D. M. Lawson, A. A. Lebedev, A. G. W. Leslie, B. Lohkamp, F. Long, M. Malý, A. J. McCoy, S. J. McNicholas, A. Medina, C. Millán, J. W. Murray, G. N. Murshudov, R. A. Nicholls, M. E. M. Noble, R. Oeffner, N. S. Pannu, J. M. Parkhurst, N. Pearce, J. Pereira, A. Perrakis, H. R. Powell, R. J. Read, D. J. Rigden, W. Rochira, M. Sammito, F. Sánchez Rodríguez, G. M. Sheldrick, K. L. Shelley, F. Simkovic, A. J. Simpkin, P. Skubak, E. Sobolev, R. A. Steiner, K. Stevenson, I. Tews, J. M. H. Thomas, A. Thorn, J. T. Valls, V. Uski, I. Usón, A. Vagin, S. Velankar, M. Vollmar, H. Walden, D. Waterman, K. S. Wilson, M. D. Winn, G. Winter, M. Wojdyr, K. Yamashita, The ıt CCP4 suite: integrative software for macromolecular crystallography. *Acta Cryst.* **D79**, 449–461 (2023).

80. E. Krissinel, K. Henrick, Inference of macromolecular assemblies from crystalline state. *J. Mol. Biol.* **372**, 774–97 (2007).

81. H. A. Delemarre-van de Waal, F. C. de Waal, [A 2d patient with tropical malaria contracted in a natural way in the Netherlands]. *Ned. Tijdschr. Geneeskd.* **125**, 375–377 (1981).

82. L. J. Robinson, R. Wampfler, I. Betuela, S. Karl, M. T. White, C. S. N. Li Wai Suen, N. E. Hofmann, B. Kinboro, A. Waltmann, J. Brewster, L. Lorry, N. Tarongka, L. Samol, M. Silkey, Q. Bassat, P. M. Siba, L. Schofield, I. Felger, I. Mueller, Strategies for understanding and reducing the Plasmodium vivax and Plasmodium ovale hypnozoite reservoir in Papua New Guinean children: a randomised placebo-controlled trial and mathematical model. *PLoS Med.* **12**, e1001891 (2015).

83. S. Okuda, Y. Watanabe, Y. Moriya, S. Kawano, T. Yamamoto, M. Matsumoto, T. Takami, D. Kobayashi, N. Araki, A. C. Yoshizawa, T. Tabata, N. Sugiyama, S. Goto, Y. Ishihama, jPOSTrepo: an international standard data repository for proteomes. *Nucleic Acids Res.* **45**, D1107–D1111 (2017).

84. Y. Perez-Riverol, C. Bandla, D. J. Kundu, S. Kamatchinathan, J. Bai, S. Hewapathirana, N. S. John, A. Prakash, M. Walzer, S. Wang, J. A. Vizcaíno, The PRIDE database at 20 years: 2025 update. *Nucleic Acids Res.* **53**, D543–D553 (2025).

Acknowledgments:

We thank Geoffrey Kong from the Monash Macromolecular Crystallisation Facility (MMCF, Clayton, VIC, Australia) for assistance with setting up the crystallization screens. This research was undertaken using the MX2 beamline at the Australian Synchrotron, part of ANSTO, and made use of the Australian Cancer Research Foundation (ACRF) detector. The authors acknowledge the use of Bio21 Advanced Microscopy Facility, WEHI CryoEM Facility and we would like to thank Andrew Leis for his support with cryo-EM sample preparation and data collection. This work was supported by the MASSIVE HPC facility (www.massive.org.au). NF54/iGP2 was kindly provided by Till Voss (Swiss Tropical and Public Health Institute). We thank Nick Walker and Pailene Lim (WEHI) for assistance with multiplex assays and sample handling. We acknowledge Professor Leanne Robinson (Burnet Institute), Benson Kiniboro and Dr Inoni Betuela (PNGIMR), and the PNGIMR Maprik field team for collection of the human study samples.

Funding:

National Health and Medical Research Council grant GNT2016908 (WHT)

National Health and Medical Research Council grant GNT2001385 (WHT)

National Health and Medical Research Council grant GNT2007996 (QG)

National Health and Medical Research Council grant GNT1173210 (RJL)

National Health and Medical Research Council grant GNT2016827 (SS)

Medical Research Future Fund grant MRFCT100006 (CWP)

CSL Centenary Fellow (AG)

Victorian State Government Operational Infrastructure Support and National Health and Medical Research Council Independent Research Institute Infrastructure Support Scheme

Author contributions:

Conceptualization: MHD, WHT

Methodology: MHD, LJC, JC, KZ, QG, SF, RSM

Formal analysis: MHD, JC, LJC, LLT, AA, TAB, LFD, RR, AA, RJL, AMV, KZ, QG, AG, SS, WHT

Investigation: MHD, JC, LJC, LLT, AA, FMTL, MG, SL, TAB, LFD, RR, AA, RM, RJL, LP, PG, MK

Resources: RJL, IM

Writing – Original draft: MHD, JC, LJC, LLT, AA, MTL, TAB, LFD, RR, RJL

Writing – reviewing and editing: All authors

Visualization: MHD, JC, LJC, LLT, AA, FMTL, RR, AA, RJL, KZ, WHT

Supervision: WHT, SL, CWP, MHD

Funding acquisition: QC, RJL, CWP, WHT

Competing interests:

Authors declare that they have no competing interests.

Data and material availability:

Cryo-EM maps have been deposited in the EM Data Bank with the following accession codes: EMD-48672 (non-uniform refinement consensus map), EMD-48669 (local refinement map of Pfs230 D1-D8), EMD-48670 (local refinement map of Pfs230 D9-D14 and Pfs48/45), and EMD-48673 (composite map). The corresponding atomic coordinates have been deposited in the Protein Data Bank with the accession codes 9MVV (Pfs230 D13D14-Pfs48/45) and 9MVT (Pfs230 D1-D8). Crystal structures have been deposited in the PDB under accession codes 9E7N (Pfs230 D13D14-W2809), 9E7O (Pfs230 D13D14-W2810) and 9E7P (Pfs230 D13D14-W2812). The SDA crosslinking mass spectrometry data have been deposited to the ProteomeXchange Consortium via jPOST(*83*) with accession number JPST003585. The mass spectrometry proteomics data have been deposited to the ProteomeXchange Consortium via the PRIDE partner repository (*84*) with the dataset identifier PXD060667. The NGS data has been deposited to the European Nucleotide Archive (ENA) under accession number PRJEB85614. All unique reagents generated in this study are available upon request to the corresponding author.

Supplementary material

Figs. S1 to S9

Tables S1 to S4

Other Supplementary Materials for this manuscript include the following:

Data S1 to S2

Fig 1. Cryo-EM structure of the Pfs230-Pfs48/45 fertilization complex shows critical sites for complex formation. (**A**) Size exclusion chromatography (SEC) profile of the purified Pfs230-Pfs48/45 complex from sexual stages of the malaria parasite. (**B**) SDS-PAGE analysis of purified Pfs230-Pfs48/45 complex corresponding to SEC fractions at retention volume 1.2-1.5 mL as indicated (panel A, black line). 1 μg of SARS-CoV-2 Spike protein was used to estimate the yield of Pfs230-Pfs48/45 complex. Pfs230 and Pfs48/45 are indicated, and molecular weight markers are on the left. (**C**) Composite map of the Pfs230-Pfs48/45 fertilization complex shown in two different views. The composite map was generated using the consensus map processed with EMReady (v2.0) and the local refinement map of the N-terminal subregion of Pfs230 (spanning D1-D8). Densities corresponding to Pfs230 (teal) and Pfs48/45 (orange) are highlighted. Left, cartoon representation of the structure placed into the cryo-EM map. Right, composite cryo-EM map colored by local resolution. (**D**) The Pfs230-Pfs48/45 binding site in two different orientations. Crosslinks consistent with the Pfs230-Pfs48/45 structure with a Cα-Cα distance less than 20 Å are indicated as black lines with orange and teal circles. Pfs230 residues that could not be placed with confidence into the density map are indicated with a dashed line in D and E. (**E**) Close-up views of the Pfs230-Pfs48/45 binding site with Pfs230 in surface representation and Pfs48/45 in cartoon representation. (F) Inter-molecular crosslinks between Pfs230 and Pfs48/45 after treatment with crosslinker sulfo-SDA. Crosslinks consistent with the Pfs230-Pfs48/45 structure with a Cα-Cα distance less than 20 Å are indicated by black lines and shown on the structures in D and E. Long distance crosslinks with a Cα-Cα distance larger than 20 Å are indicated by grey lines.

Fig 2. Tertiary fold of the endogenous Pfs230-Pfs48/45 fertilization complex. (**A**) Structure of the Pfs230-Pfs48/45 complex with the individual 6-cysteine domains indicated. Pfs230 and Pfs48/45 are colored in shades of teal and orange, respectively. The glycosylphosphatidylinositol anchor of Pfs48/45 is shown as GPI. (**B**) Simplified model of the Pfs230-Pfs48/45 complex organization. The center of mass of each 6-cysteine domain is represented by a centroid. (**C**) Stacking of multiple consecutive 6-cysteine domains in Pfs230 D1 to D6 with panel i showing a close-up view of Pfs230 D6 to D9. (**D**) Stacking of multiple consecutive 6-cysteine domains in Pfs230 D9 to D14 with panels i-iii showing the contacts of the central 6-cysteine domains D10, D11 and D13. (**E**) Tandem 6-cysteine domains of Pfs230 were aligned and shown in the same orientation next to each other. The center of mass of each domain is indicated by a black line and angles between tandem domain pairs are indicated. (**F**) Previously published crystal structures of 6-cysteine proteins containing two or three 6-cysteine domains with the PDB ID indicated. The center of mass of each domain and angles between tandem domain pairs are indicated.

Fig 3. Domains 13 and 14 of Pfs230 are critical for the localization of Pfs230 on *P. falciparum* gametes. (**A**) Immunoblotting analyses using anti-Pfs230 LMIV230-01, anti-FLAG and anti-StrepII antibodies show that 230ΔD13D14 line expresses a truncated Pfs230, which runs at a lower molecular weight than the full-length protein present in 230FL. Both lines express C-terminal 3xFLAG and TwinStrepII tags. Anti-HSP70 was used as a loading control. All samples were run in non-reducing conditions. Molecular weight markers are shown on the left. (**B**) Immunofluorescence assay of stage V gametocytes from NF54/iGP2 expressing full-length Pfs230 or 230Δ1314. Fixed gametocytes were stained with anti-Pfs48/45 TB31F conjugated to Alexa 647 and anti-Pfs230 LMIV230-01 directly conjugated to Alexa 555. Parasite nuclei are stained with DAPI (cyan), merged and bright field (BF) images are shown. Scale bar = 5 μm. (**C**) Surface immunofluorescence assay (SIFA) of activated macrogametes (left panel) and microgametes (right panel) of NF54/iGP2 which express full length Pfs230 and two clonal lines of 230ΔD13D14. Gametes were stained with anti-Pfs48/45 TB31F conjugated to Alexa 647 and anti-Pfs230 LMIV230-01 directly conjugated to Alexa 555 prior to fixation. Merged and bright field (BF) images are shown. Scale bar = 5 μm. (**D**) Automated quantitation of Pfs230 localization observed in the SIFA of activated macrogametes, where anti-Pfs230 staining was classified as either being colocalized with anti-P48/45 staining (black) or absent while Pfs48/45 was staining was present (grey). The number of activated macrogametes counted for each parasite line is shown above each stacked bar graph. (**E**) SMFA assessing the transmissibility of NF54/iGP2 and two clonal lines of 230Δ1314 (G6 and F4). Number of oocysts per dissected midgut is plotted for two experiments. Bars show the mean and standard deviation. N, number of uninfected mosquitoes / total number of mosquitoes.

Fig 4. Nanobodies specific to Pfs230 D13D14 recognize gametocytes, block complex formation and reduce oocyst numbers in mosquitoes. (**A**) Nanobody binding to Pfs230 D13D14 was evaluated by ELISA. (**B**) Cladogram of the 100 most abundant nanobodies from Next-Generation Sequencing (NGS) with nanobodies identified by Sanger sequencing labelled. Tree tips are scaled relative to abundance. (**C**) Biolayer interferometry (BLI) affinity measurements for nanobody affinities. Measurements were plotted (solid line) and fitted to a 1:1 binding model (dashed line). Mean K_D values for replicates with standard deviations are shown. (**D**) Epitope binning using BLI. The green and white boxes represent non-competition and competition, respectively. (**E**) Binding specificity of nanobodies to different Pfs230 domains and Pvs230 D13D14 by BLI. Representative curves of two independent experiments. (**F**) Immunofluorescence assay of stage V gametocytes using the indicated nanobody (Nb) detected with goat anti-alpaca IgG VHH domain conjugated to Alexa Fluor 488 (magenta) and anti-Pfs230 LMIV230-01 antibody conjugated to Alexa 555 (yellow). Parasite nuclei are stained with DAPI (cyan), merged and brightfield (BF) images are shown. Scale bar = 5 μm. (**G**) Pull-down of Pfs230-Pfs48/45 complex from parasite lysate in the presence of various antibodies or nanobody-Fcs examined using immunoblotting under non-reducing conditions. Pfs48/45 and Pfs230 are indicated on the right. Representative blots of n = 3 independent experiments. I, input; U, unbound; E, eluate. Molecular weight ladder labeled on the left in kDa. (**H**) Transmission-blocking activity of anti-Pfs230 D13D14 nanobody-Fcs by SMFA. Oocysts/midgut are plotted for three experiments. Nanobody-Fcs were at a concentration of 100 μg/mL (experiment 1 and 2) and 200 μg/mL (experiment 3). LMIV230-01 was added at 200 μg/mL in all experiments. Bars show means with standard deviation. TRA, transmission reducing activity; N, number of uninfected mosquitoes / total number of mosquitoes.

Fig 5. Structural analyses of Pfs230 D13D14 nanobodies that inhibit Pfs230-Pfs48/45 complex formation. (**A**) Pfs230 D13D14/W2809 complex at 2.5 Å, Pfs230 D13D14/W2810 complex at 1.9 Å and Pfs230 D13D14/W2812 complex at 3.2 Å resolution. Pfs230 D13D14 is shown in teal and nanobodies W2809, W2810 and W2812 are shown in purple, beige and pink, respectively. (**B**) Surface representation of Pfs230 D13D14 showing the epitope footprint of residues within 4 Å of the nanobodies, with W2809, W2810 and W2812 shown in purple, beige and pink, respectively. (**C**) Cryo-EM structure of Pfs230 D9 to D14 and Pfs48/45 is shown in two orientations, with Pfs230 domains D13 and D14 shown in surface representation (white) and domains D9 to D12 in cartoon representation (teal). The epitope footprint of W2809, W2810 and W2812 is shown in purple, beige and pink, respectively. (**D**) TB31F and Pfs230 clash for binding to Pfs48/45. Overlay of PDB ID 6E63 with cryo-EM structure of Pfs230 D13D14-Pfs48/45. TB31F Fab is shown in grey in surface representation. (**E**) Overlapping binding sites of Pfs230 and TB31F Fab on D3 of Pfs48/45. Pfs48/45 is shown in surface representation with Pfs230 and TB31F footprints in teal and light grey, respectively.

Fig 6. Pfs230 D13D14 is a target of naturally acquired immunity and a potential transmission-blocking vaccine candidate. (**A**) Schematic of full-length Pfs230 with respective recombinant fragments indicated. SP, Signal peptide. (**B**) Multiplex assay for plasma reactivity against P230 domains from PNG individuals with current *P. falciparum* infection (Pf pos), prior infection (Pf prior) or naïve individuals. Dashed line, antigen-specific seropositivity cut-off. Statistical significance between groups was calculated using a Kruskal-Wallis test, with Dunn's multiple comparisons test. * $p \leq 0.05$, ** $p \leq 0.01$, *** $p \leq 0.001$, **** $p \leq 0.0001$. (**C**) Groups of C57BL/6 mice were immunized with either 230D13D14L or 230D13D14S mRNA-LNP. Mice were immunized (IM) on days 1 and 28. For pre-immune sera, mice were bled on day 1 prior to immunization. Immunized mice were subsequently bled on day 21 (B1) and 68 (B2). Pfs230 D13D14 end point antibody levels were measured. Error bars represent 95% confidence intervals of the geometric mean. n = 6 mice per immunization group. (**D**) Immuno blot analyses showing immunized mouse sera are specific to Pfs230 D13D14 in gametocytes. Anti-HSP70, loading control. Molecular weight markers, left. (**E**) Immunofluorescence assay of stage V gametocytes from NF54/iGP2 expressing full-length Pfs230 and 230Δ1314. Fixed gametocytes were stained with pre-immune or second bleed pooled sera from mice immunized with 230D13D14S mRNA-LNP. (**F**) SIFA of macrogametes stained with pre-immune or second bleed pooled sera from mice immunized with 230D13D14S mRNA-LNP. Anti-Pfs230 LMIV230-01 was directly conjugated to Alexa 555. Parasite nuclei were stained with DAPI (cyan), merged and bright field (BF) images are shown. Scale bar = 5 μm. (**G**) SMFA using either pre-immune or second bleed following immunization with 230D13D14S or 230D13D14L mRNA-LNP. Number of oocysts per dissected midgut are plotted for three experiments, experiment 3 included complement active human serum. Bars show means and standard deviation. TRA, transmission reducing activity; N, number of uninfected mosquitoes / total number of mosquitoes. Mean, mean number of oocysts per midgut.

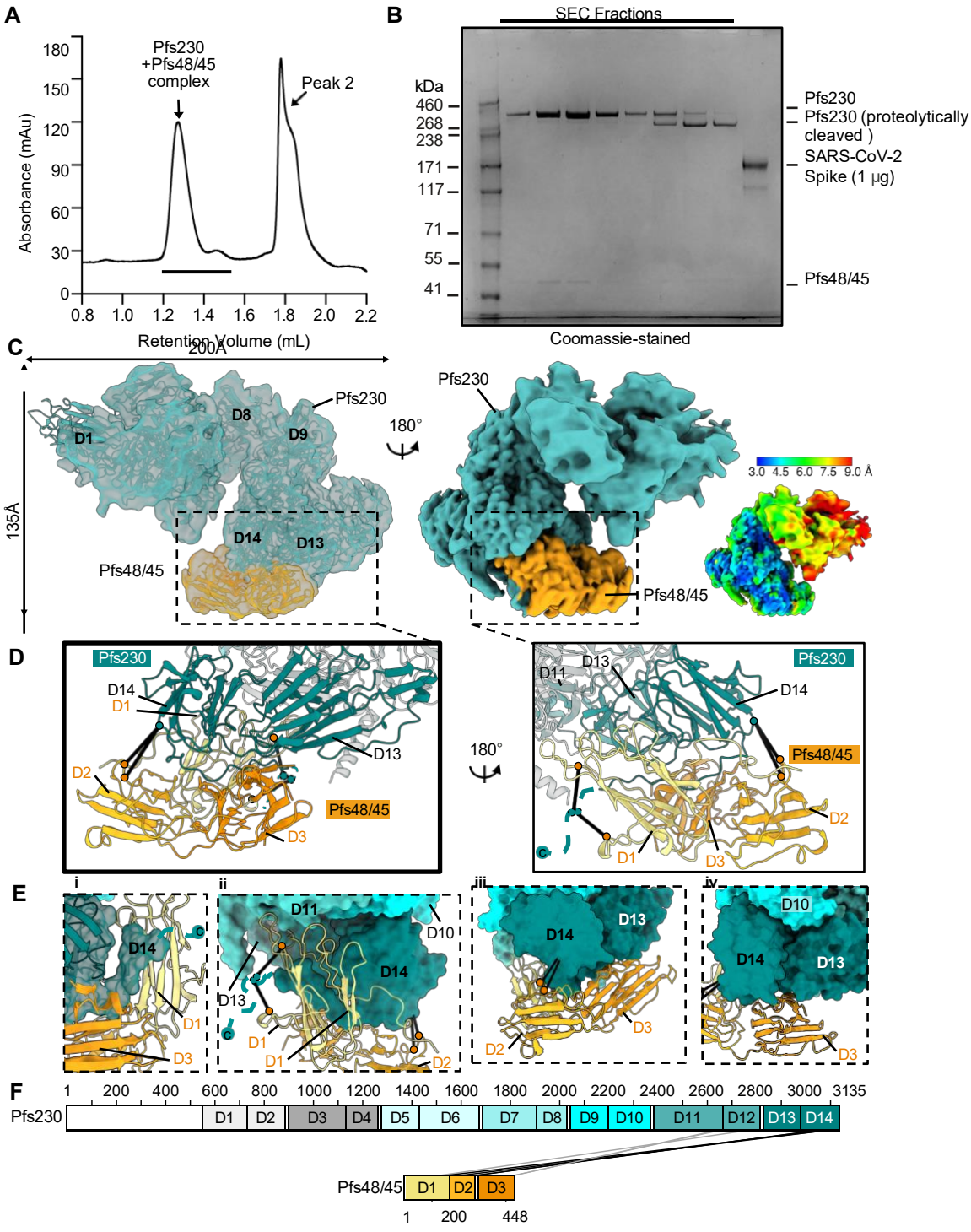
A
Pfs230
+Pfs48/45
complex
Peak 2
Absorbance (mAu)
Retention Volume (mL)
B
SEC Fractions
kDa
460
268
238
171
117
71
55
41
Pfs230
Pfs230 (proteolytically cleaved)
SARS-CoV-2 Spike (1 µg)
Pfs48/45
Coomassie-stained
C
200Å
135Å
Pfs230
D8
D9
D1
D14
D13
Pfs48/45
180°
3.0 4.5 6.0 7.5 9.0 Å
D
Pfs230
D14
D1
D2
D13
Pfs48/45
D3
180°
D11
E
i
ii
iii
iv
D10
F
Pfs230
D1
D2
D3
D4
D5
D6
D7
D8
D9
D10
D11
D12
D13
D14
Pfs48/45
1
200
448

Figure 1

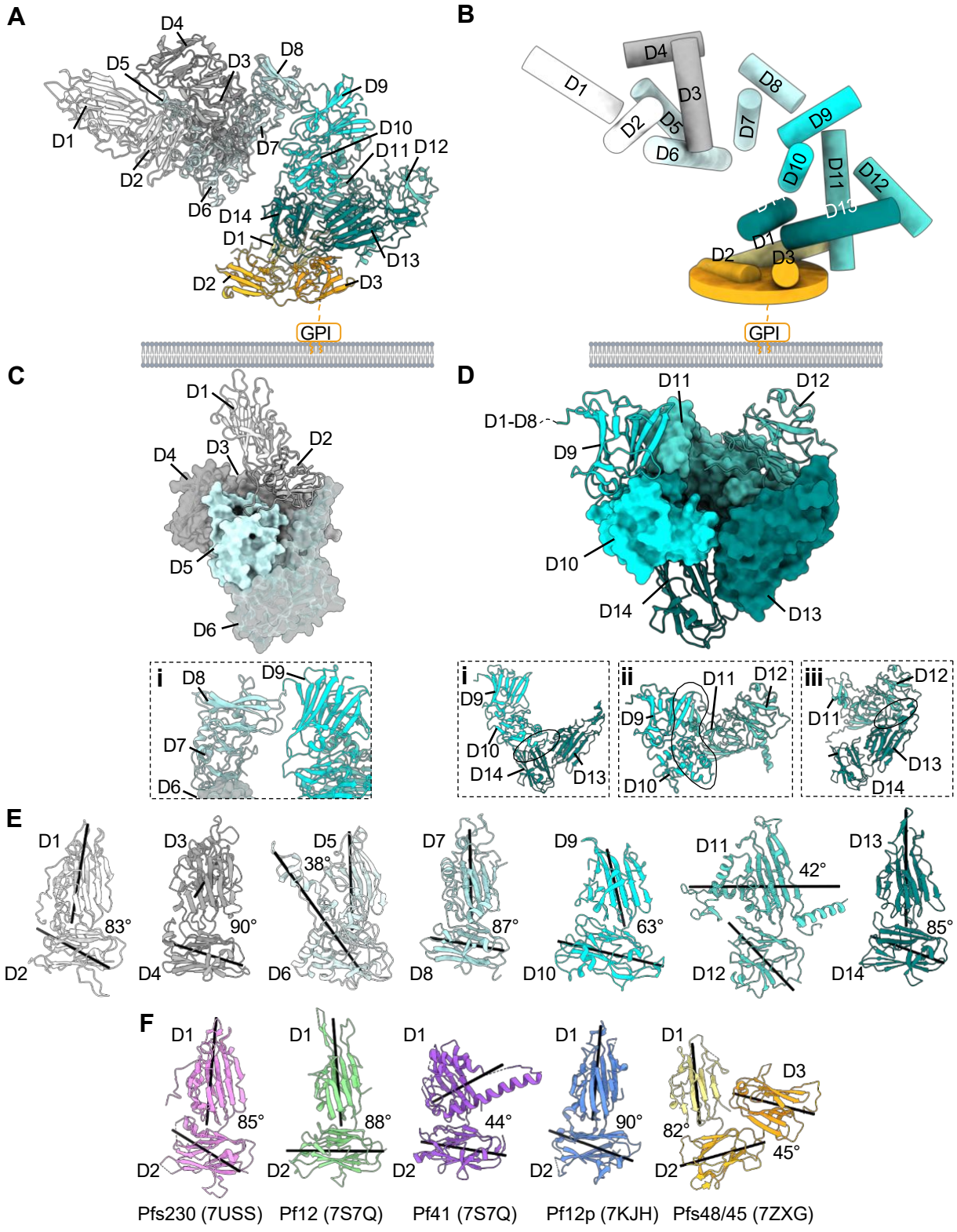
A
B
C
D
E
F
GPI
GPI
D1-D8
Pfs230 (7USS)
Pf12 (7S7Q)
Pf41 (7S7Q)
Pf12p (7KJH)
Pfs48/45 (7ZXG)

Figure 2

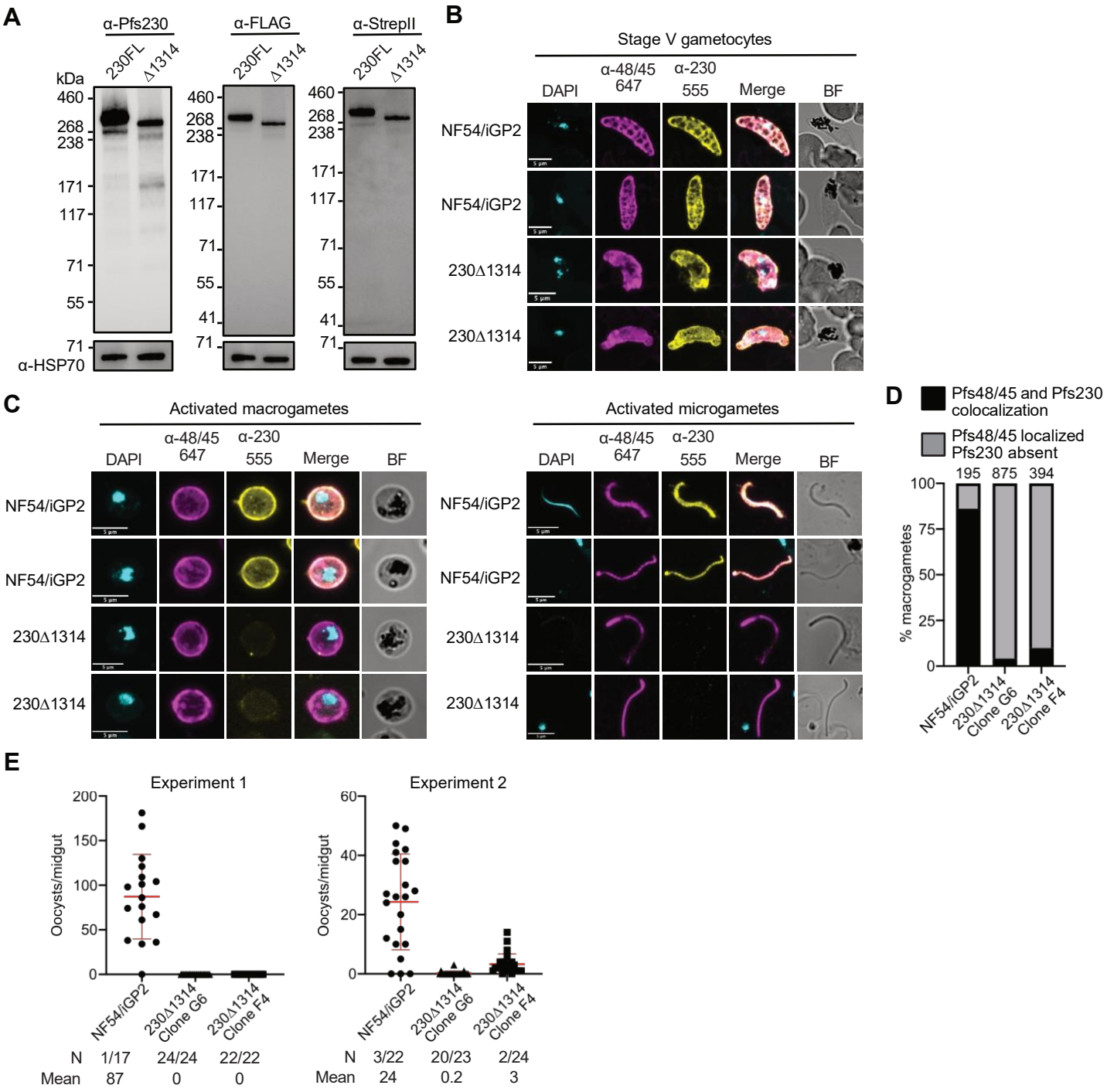
A
α-Pfs230
α-FLAG
α-StrepII
230FL
Δ1314
kDa
460
268
238
171
117
71
55
41
α-HSP70
B
Stage V gametocytes
DAPI
α-48/45 647
α-230 555
Merge
BF
NF54/iGP2
230Δ1314
C
Activated macrogametes
Activated microgametes
D
Pfs48/45 and Pfs230 colocalization
Pfs48/45 localized Pfs230 absent
% macrogametes
195
875
394
NF54/iGP2
230Δ1314 Clone G6
230Δ1314 Clone F4
E
Experiment 1
Experiment 2
Oocysts/midgut
N 1/17 24/24 22/22
Mean 87 0 0
N 3/22 20/23 2/24
Mean 24 0.2 3

Figure 3

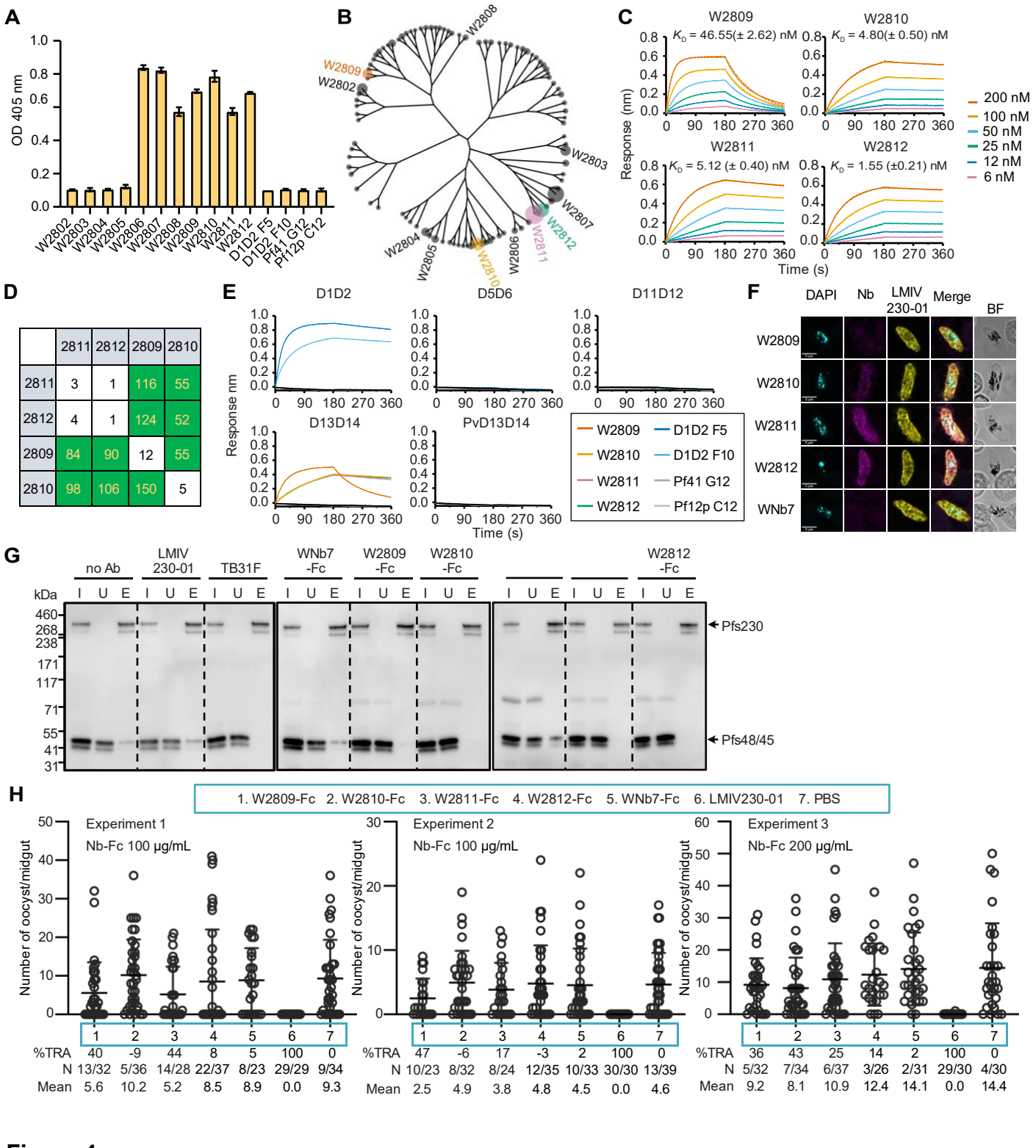
A
OD 405 nm
W2802
W2803
W2804
W2805
W2806
W2807
W2808
W2809
W2810
W2811
W2812
D1D2 F5
D1D2 F10
Pf41 G12
Pf12p C12
B
C
W2809
W2810
W2811
W2812
Response (nm)
Time (s)
200 nM
100 nM
50 nM
25 nM
12 nM
6 nM
D
2811 2812 2809 2810
2811 3 1 116 55
2812 4 1 124 52
2809 84 90 12 55
2810 98 106 150 5
E
D1D2
D5D6
D11D12
D13D14
PvD13D14
Response nm
Time (s)
W2809
W2810
W2811
W2812
D1D2 F5
D1D2 F10
Pf41 G12
Pf12p C12
F
DAPI
Nb
LMIV 230-01
Merge
BF
W2809
W2810
W2811
W2812
WNb7
G
no Ab
LMIV 230-01
TB31F
WNb7 -Fc
W2809 -Fc
W2810 -Fc
W2812 -Fc
kDa
I U E
460
268
238
171
117
71
55
41
31
Pfs230
Pfs48/45
H
1. W2809-Fc 2. W2810-Fc 3. W2811-Fc 4. W2812-Fc 5. WNb7-Fc 6. LMIV230-01 7. PBS
Experiment 1
Nb-Fc 100 µg/mL
Experiment 2
Nb-Fc 100 µg/mL
Experiment 3
Nb-Fc 200 µg/mL
Number of oocyst/midgut
%TRA 40 -9 44 8 5 100 0
N 13/32 5/36 14/28 22/37 8/23 29/29 9/34
Mean 5.6 10.2 5.2 8.5 8.9 0.0 9.3
%TRA 47 -6 17 -3 2 100 0
N 10/23 8/32 8/24 12/35 10/33 30/30 13/39
Mean 2.5 4.9 3.8 4.8 4.5 0.0 4.6
%TRA 36 43 25 14 2 100 0
N 5/32 7/34 6/37 3/26 2/31 29/30 4/30
Mean 9.2 8.1 10.9 12.4 14.1 0.0 14.4

Figure 4

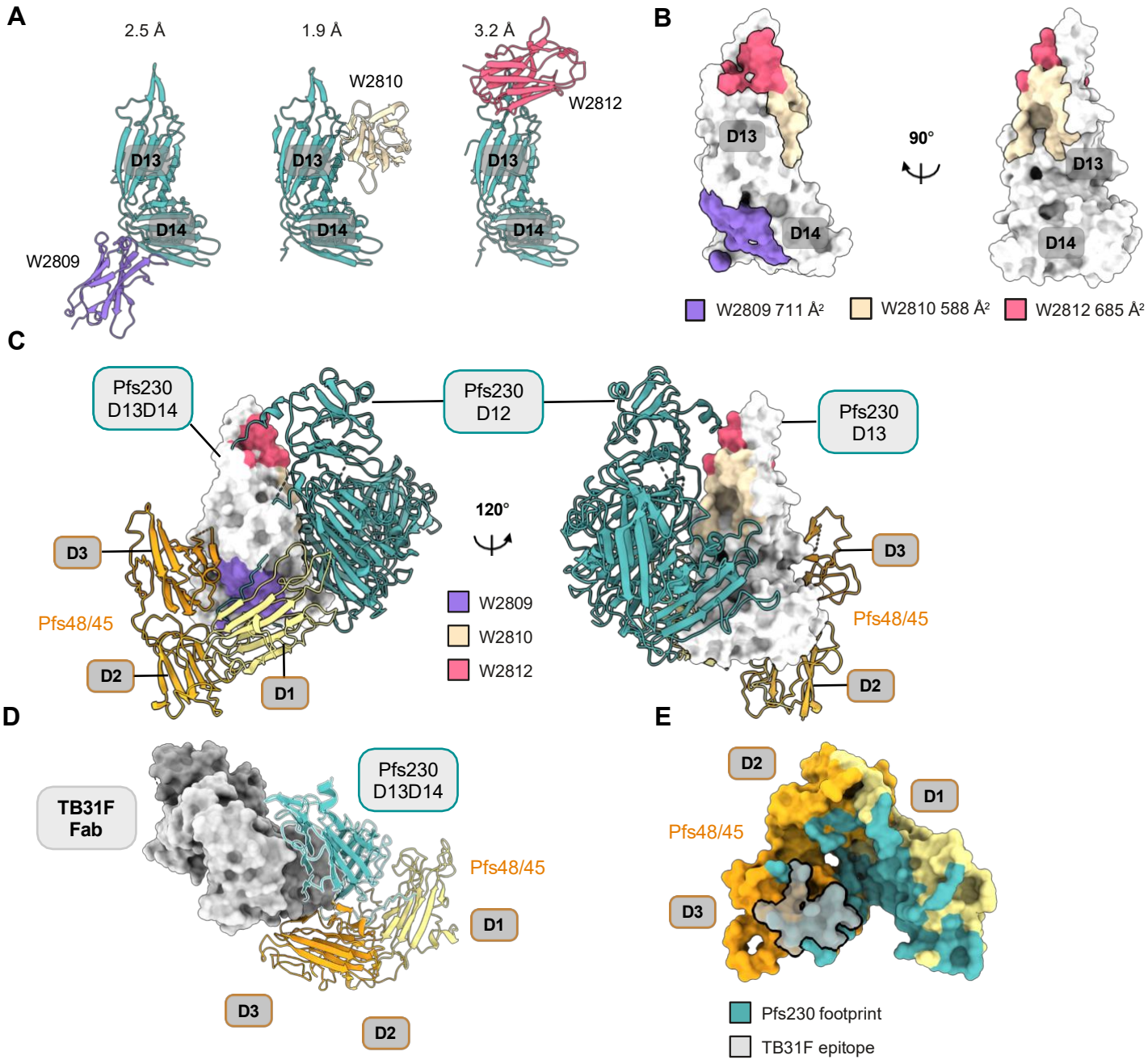
A
2.5 Å
1.9 Å
3.2 Å
W2810
W2812
D13
D14
W2809
B
90°
W2809 711 Å²
W2810 588 Å²
W2812 685 Å²
C
Pfs230 D13D14
Pfs230 D12
Pfs230 D13
120°
D3
Pfs48/45
D2
D1
W2809
W2810
W2812
D
TB31F Fab
Pfs230 D13D14
Pfs48/45
D1
D3
D2
E
D2
D1
Pfs48/45
D3
Pfs230 footprint
TB31F epitope

Figure 5

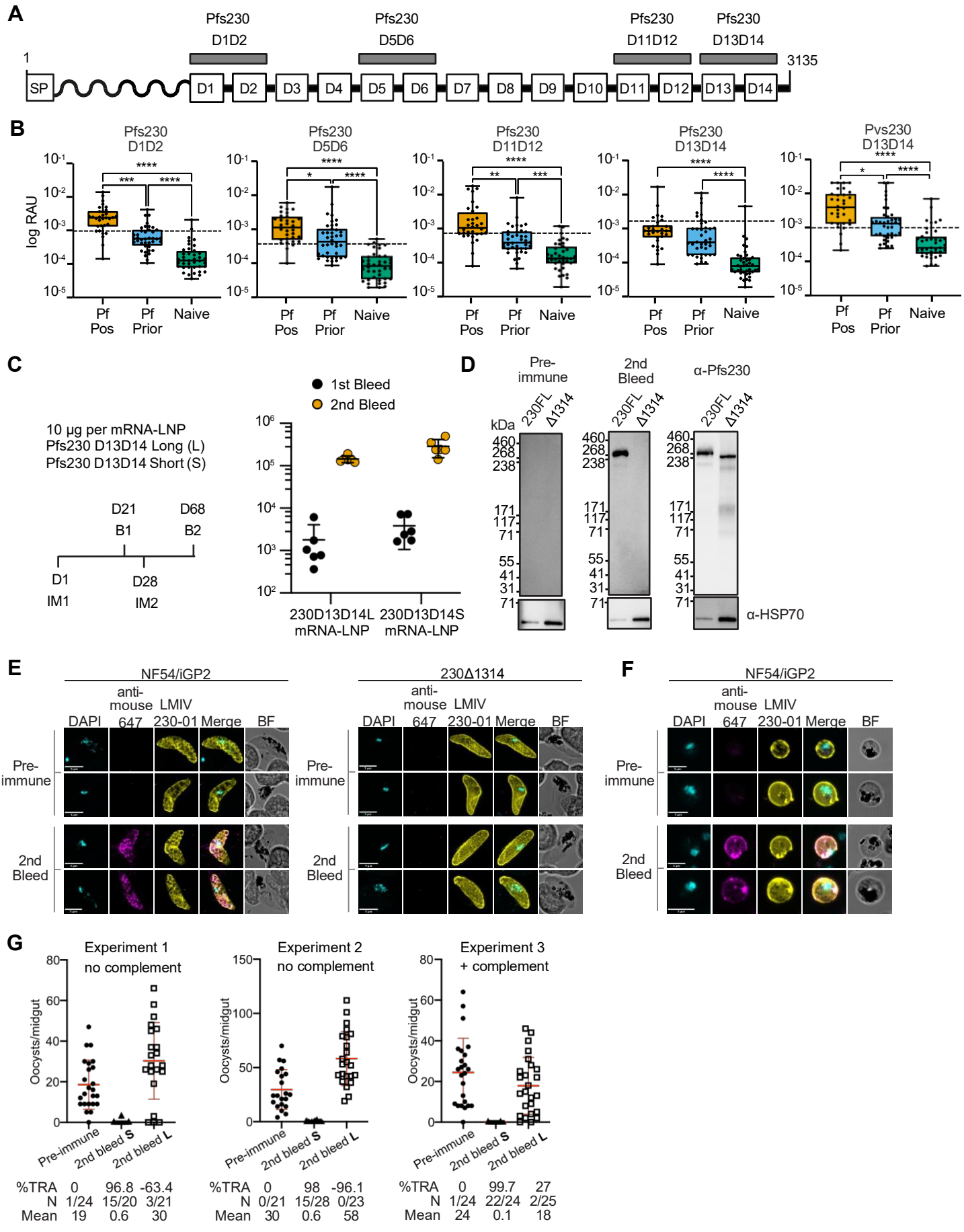
A
Pfs230 D1D2
Pfs230 D5D6
Pfs230 D11D12
Pfs230 D13D14
1
3135
SP
D1
D2
D3
D4
D5
D6
D7
D8
D9
D10
D11
D12
D13
D14
B
Pfs230 D1D2
Pfs230 D5D6
Pfs230 D11D12
Pfs230 D13D14
Pvs230 D13D14
log RAU
Pf Pos
Pf Prior
Naive
C
10 µg per mRNA-LNP
Pfs230 D13D14 Long (L)
Pfs230 D13D14 Short (S)
D21
D68
B1
B2
D1
D28
IM1
IM2
1st Bleed
2nd Bleed
230D13D14L mRNA-LNP
230D13D14S mRNA-LNP
D
Pre-immune
2nd Bleed
α-Pfs230
kDa
230FL
Δ1314
α-HSP70
E
NF54/iGP2
230Δ1314
anti-mouse 647
LMIV 230-01
DAPI
Merge
BF
Pre-immune
2nd Bleed
F
NF54/iGP2
G
Experiment 1
no complement
Experiment 2
no complement
Experiment 3
+ complement
Oocysts/midgut
Pre-immune
2nd bleed S
2nd bleed L
%TRA 0 96.8 -63.4
N 1/24 15/20 3/21
Mean 19 0.6 30
%TRA 0 98 -96.1
N 0/21 15/28 0/23
Mean 30 0.6 58
%TRA 0 99.7 27
N 1/24 22/24 2/25
Mean 24 0.1 18

Figure 6

Science
AAAS

Supplementary Materials for

Cryo-EM structure of endogenous *Plasmodium falciparum* Pfs230 and Pfs48/45 fertilization complex

Melanie H. Dietrich[1,2], Jill Chmielewski[1,2], Li-Jin Chan[1,2], Li Lynn Tan[1], Amy Adair[1], Frankie M. T. Lyons[1,2], Mikha Gabriela[1,2], Sash Lopaticki[1,3], Toby A Dite[1,2], Laura F Dagley[1,2], Lucia Pazzagli[4], Priya Gupta[4], Mohd Kamil[4], Ashley M. Vaughan[4,5], Rattanaporn Rojrung[6], Anju Abraham[1], Ramin Mazhari[1,2], Rhea J. Longley[1,2,7], Kathleen Zeglinski[1,2], Quentin Gouil[1,2,8,9], Ivo Mueller[1,2,10], Stewart A. Fabb[11], Rekha Shandre-Mugan[11], Colin W. Pouton[11], Alisa Glukhova[1,2,12,13,14], Shabih Shakeel[1,2,12,14] and Wai-Hong Tham[1,2,15*]

Corresponding author: tham@wehi.edu.au

The PDF file includes:

Figs. S1 to S9
Tables S1 to S4

Other Supplementary Materials for this manuscript include the following:

Data S1 to S2

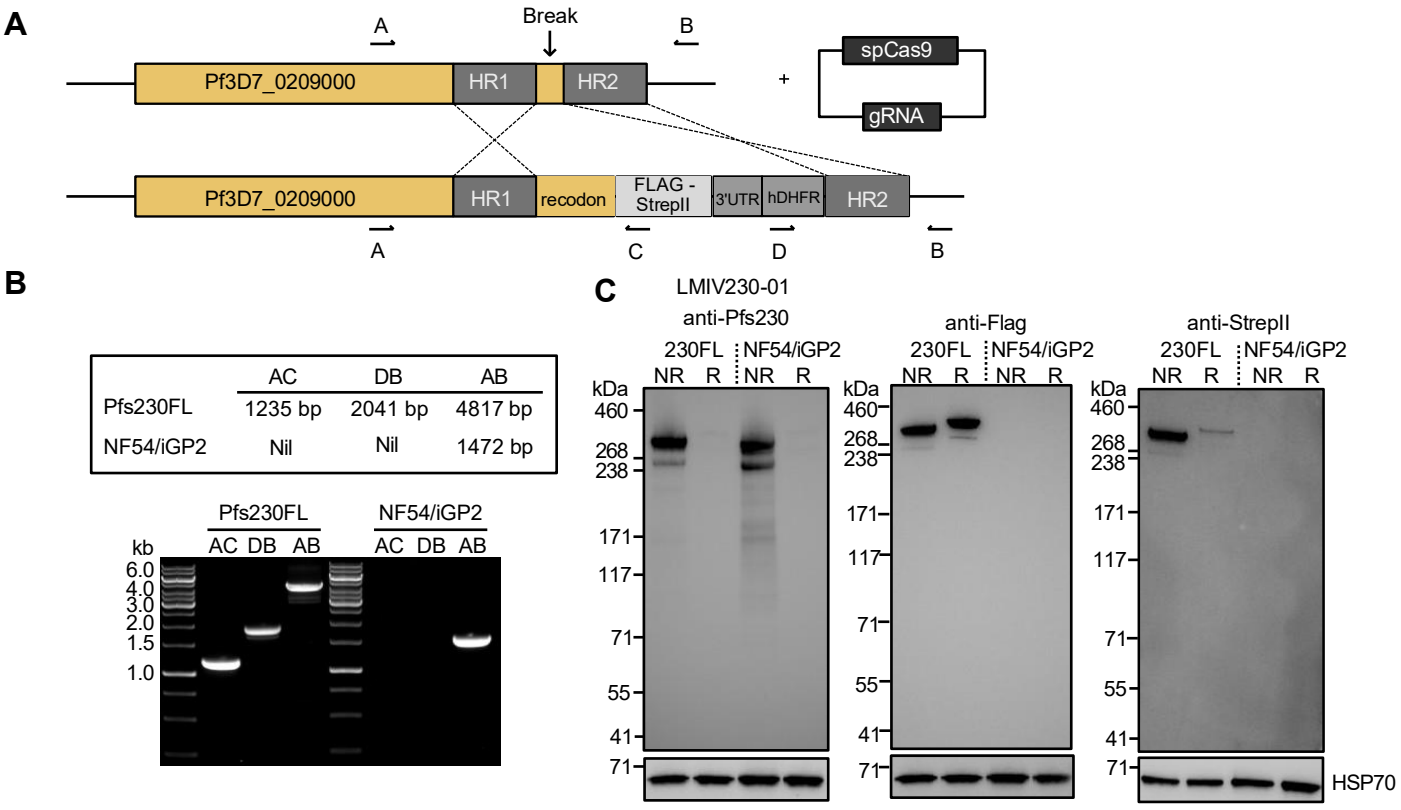

Figure S1. Transgenic *P. falciparum* line expressing Pfs230 with a C-terminal 3xFLAG-TwinStrepII tag
(A) Schematic illustrating the strategy for generation of the Pfs230-3xFLAG-TwinStrepII line in an NF54/iGP2 background. This transgenic line is referred to as Pfs230FL. Genotyping primers (A, B, C and D) are indicated in the schematic. gRNA, guide RNA; HR, homology region; hDHFR, human dihydrofolate reductase; recodon, recodonized; SpCas9, *Streptococcus pyogenes* Cas9; UTR, untranslated region. 5' and 3' homology regions are indicated as HR1 and HR2, respectively. (B) Expected amplicon sizes are shown in relation to the respective genotyping primer pairs. Gel electrophoresis of the PCR amplicons is shown for both the transgenic Pfs230FL and the parental NF54/iGP2 lines. DNA ladder sizes are shown on the left. (C) Western blot of transgenic Pfs230FL and the parental line NF54/iGP2 using anti-Pfs230 LMIV230-01, anti-FLAG and anti-StrepII antibodies, showing expression of the 3xFLAG and TwinStrepII tag on Pfs230. Pfs230 is present as 360 kDa and 310 kDa bands, with the lower band representing proteolytically cleaved Pfs230. Anti-HSP70 was used as a loading control. Non-reducing and reducing conditions are shown as NR and R, respectively. Molecular weight markers are shown on the left.

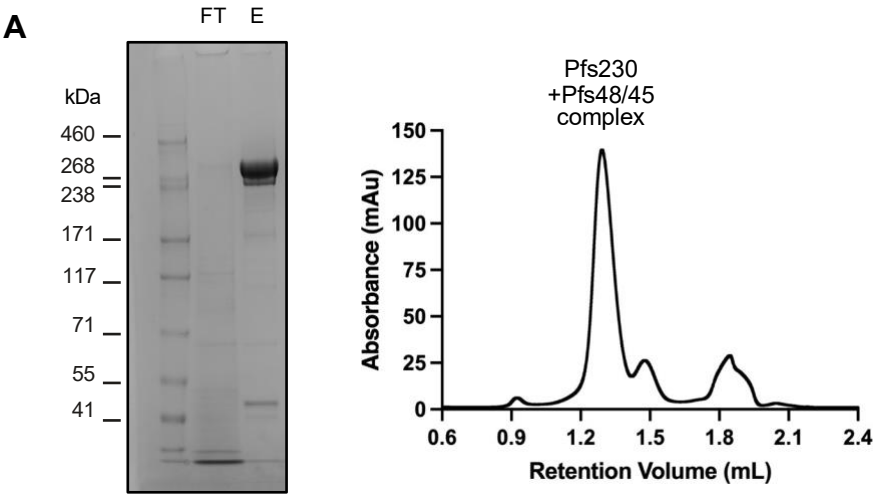

Protein IDs	Gene names	Mol. weight [kDa]	Peptides	Unique peptides	Sequence coverage %	Intensity
A0A143ZY09	Pfs230	363.2	424	424	75.5	774380000
A0A5K1K917;Q8I6T1	Pfs45/48	51.5	20	20	39.1	4979700
Q8I2X4	HSP70	72.4	26	26	49.2	1585800

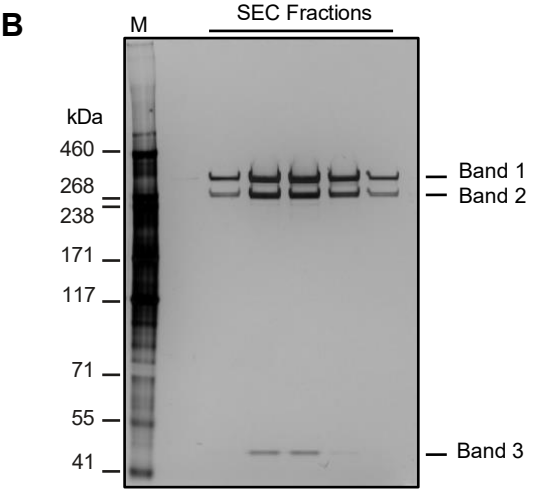

Band	Gene names	Mol. weight [kDa]	Peptide counts
Band 1	Pfs230	363.2	192
Band 2	Pfs230	363.2	192
Band 3	Pfs48/45	51.5	6

Figure S2. Mass spectrometry analyses confirm purification of endogenous Pfs230-Pfs48/45 fertilization complex

(A) Coomassie-stained SDS-PAGE gel showing the purification of endogenous Pfs230-Pfs48/45 complex from Pfs230FL using StrepTactin XT resin with the flowthrough (FT) and elution (E) shown. Right panel shows the SEC fractions that correspond with the Pfs230-Pfs48/45 complex. The mass spectrometry analyses show the top three hits with more than three unique peptides from in solution digest preparation. (B) Silver-stained SDS-PAGE gel showing the purification of endogenous Pfs230-Pfs48/45 complex from a Pfs230-HA tagged line using anti-HA, with the relevant SEC fractions shown. Right panel shows the mass spectrometry analyses of the top hit from each band from in gel digest preparation.

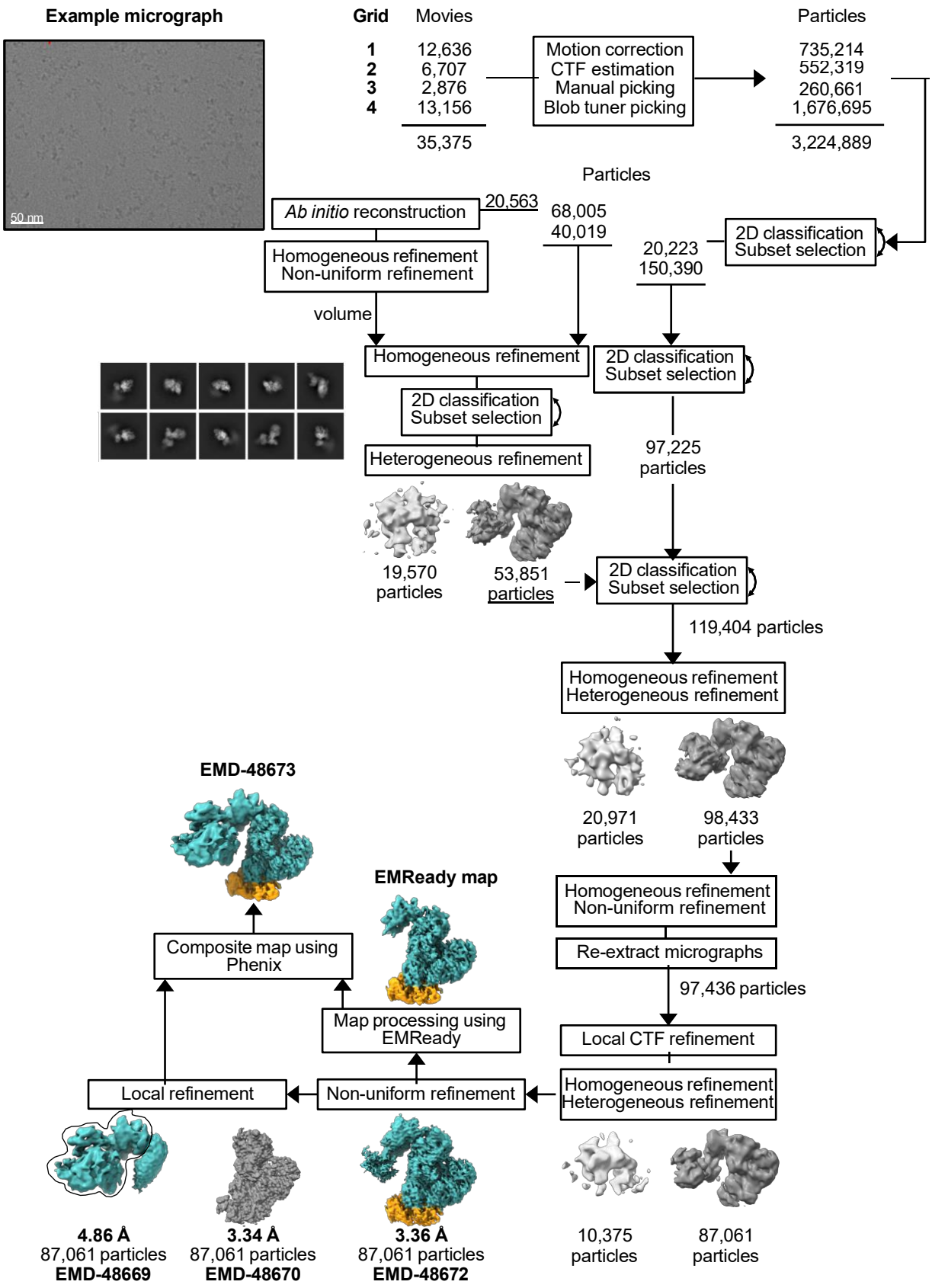

Figure S3. Workflow for cryo-EM data processing

Movies from four grids of Pfs230-Pfs48/45 complex after size exclusion chromatography were pre-processed separately in cryoSPARC v4.6.0. Manual particle picking was followed by Blob Tuner Picking. After 2D classification, particles of one grid were used for ab initio reconstruction. Particle stacks of the other grids were added at the 2D classification step and further refined using heterogeneous refinement and local contrast transfer function (CTF) refinement. A non-uniform refinement was used to obtain the consensus map of the complex (EMD-48672). The map was further locally refined to improve the map of the lower resolution part of Pfs230 (domains 1-8, EMD-48669) and the higher resolution part containing Pfs230 domains 9-14 and Pfs48/45 (EMD-48670) using soft masks around the regions of interest. EMReady (v2.0) was used to further improve the quality of the non-uniform refinement consensus map (EMD-48672). A composite map (EMD-48673) was generated from the EMReady processed consensus map and the local refinement map of Pfs230 domains 1-8 (EMD-48669) using Phenix (v1.21.1). The EMReady map in the figure refers to EMReady processed consensus map.

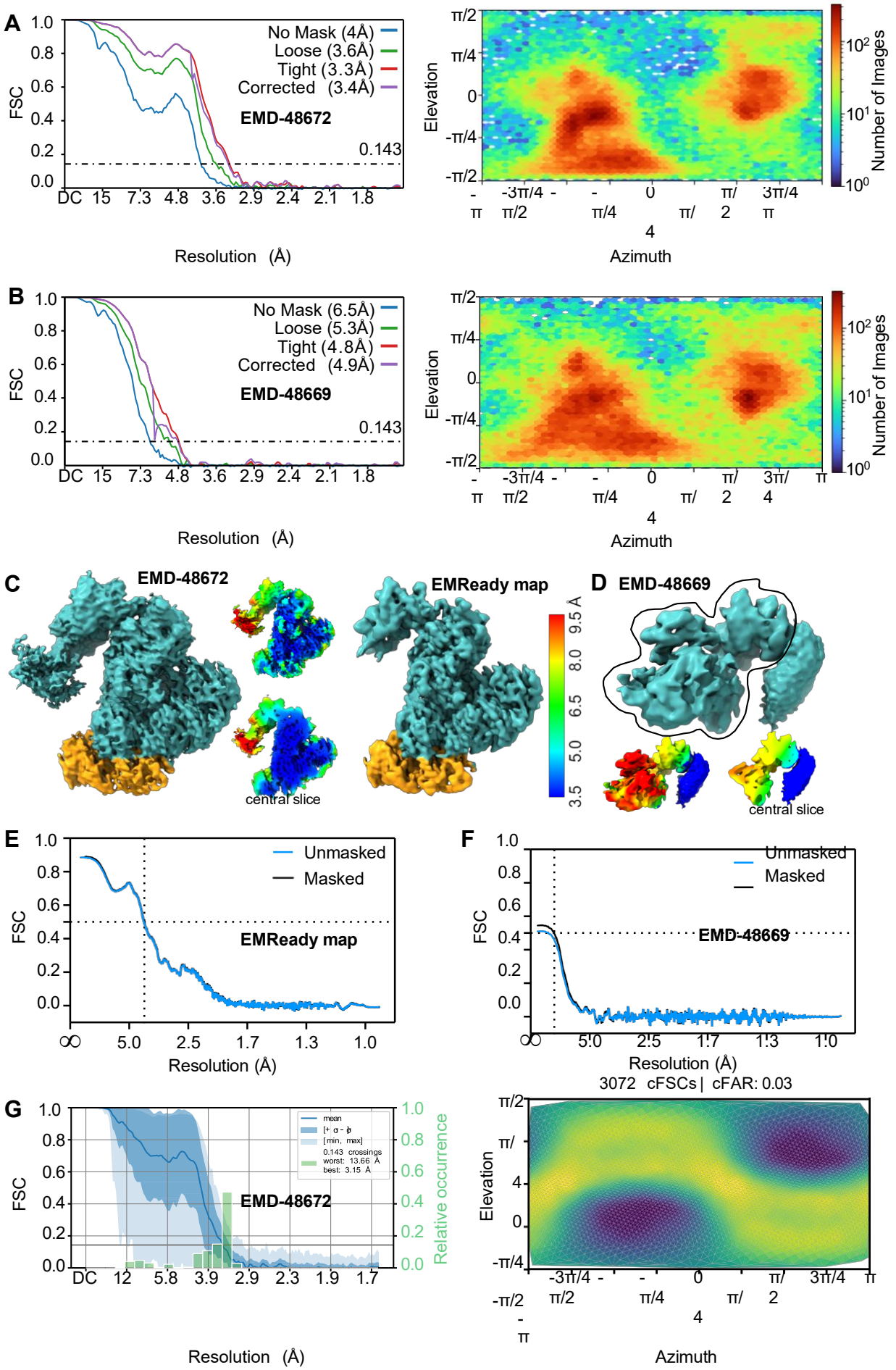

Figure S4. Cryo-EM processing statistics

(A) Gold-Standard Fourier shell correlation (FSC) curves of the consensus Pfs230-Pfs48/45 reconstruction (EMD-48672) and its particle view distribution plot. (B) Gold-Standard FSC curves of the local refinement map corresponding to Pfs230 D1 to D8 reconstruction (EMD-48669) and its particle view distribution plot. (C) Consensus map after non-uniform refinement (EMD-48672) and its corresponding EMReady map post processing. (D) Local refinement map of the Pfs230 D1 to D8 region (EMD-48669). Surrounding trace indicates mask used for local refinement. Particle stacks were not subtracted. (C-D) Cryo-EM maps coloured by local resolution are shown for each processed map in the same orientation as well as centrally sliced. (E)

Model vs map FSC curves of Pfs230 D9 to D14-Pfs48/45 model with EMReady map. (F) Model vs map FSC curves for model comprising Pfs230 D1 to D8 with local refinement map (EMD-48669). (G) Conical FSC summary plot (left) and cFAR plot (right) of consensus map (EMD-48672). The EMReady map in the figure refers to EMReady processed consensus map.

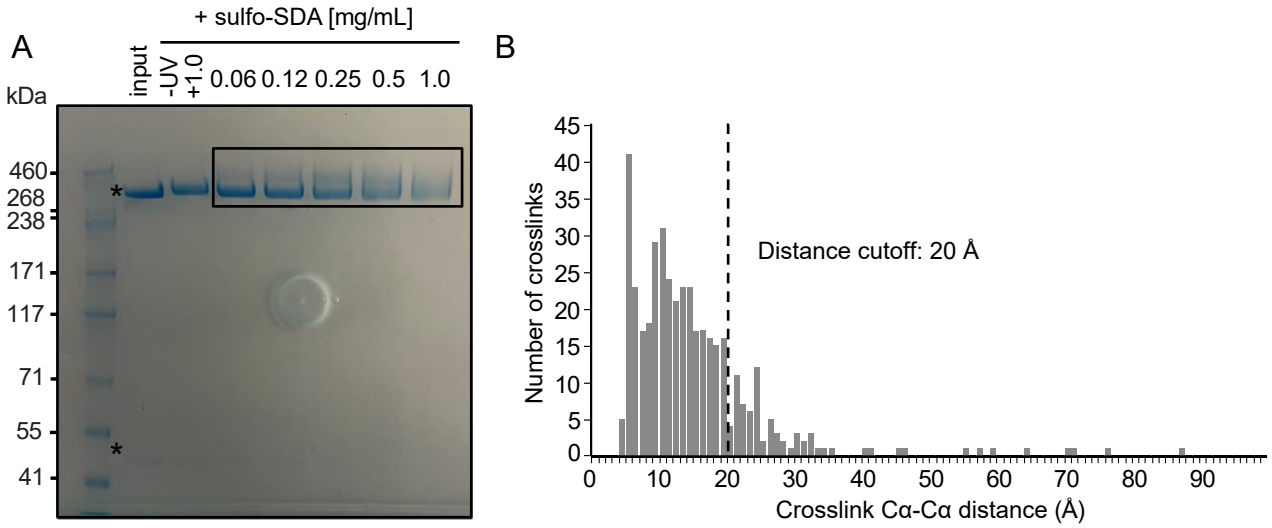

Figure S5. Crosslinking mass spectrometry of the Pfs230-Pfs48/45 complex
(A) SDS-PAGE gel of purified Pfs230-Pfs48/45 complex without crosslinker (input), and after incubation with crosslinker Sulfo-SDA at different concentrations and UV exposure. Pfs230 and Pfs48/45 bands are indicated (*) at 360 and 50 kDa, respectively, in the input sample. Covalent linkage of the two proteins results in protein bands at a higher molecular weight. Rectangular box indicates bands used for mass spectrometry. (B) Histogram showing the distance distribution of crosslinks using the structural model of Pfs230-Pfs48/45. The line at 20 Å indicates the distance cutoff for links classified as long-distance. 82% of crosslinks fall within the crosslinker specific distance cutoff.

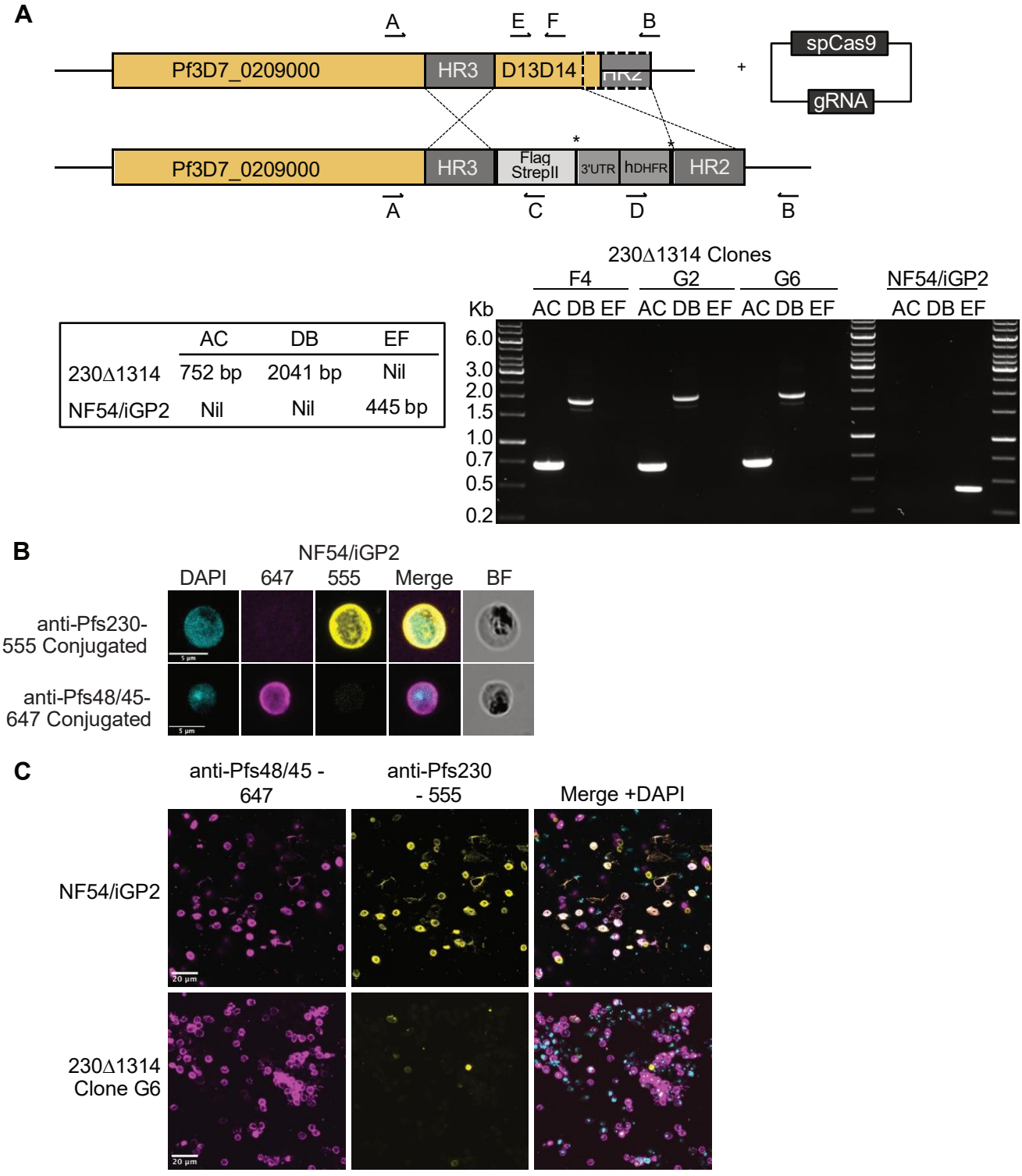

Figure S6. Generation of transgenic 230Δ1314 and localization of Pfs230 in activated macrogametes
(A) Schematic illustrating the strategy for generation of transgenic 230Δ1314 with 3xFLAG-TwinStrepII in NF54/iGP2 background. Genotyping primers are indicated in the schematic. Expected amplicon sizes are shown in relation to the respective genotyping primer pairs (bottom panel, left). Gel of the PCR amplicons is shown for both the transgenic 230Δ1314 and the parental line NF54/iGP2 lines (bottom panel, right). DNA ladder sizes are shown on the left. (B) Representative surface immunofluorescence assay (SIFA) images of NF54/iGP2 macrogametes which express full-length Pfs230 stained individually with anti-Pfs48/45 conjugated to 647 and anti-Pfs230 conjugated to 555 show no cross-over fluorescence. DAPI, merge and bright field (BF) images are shown. Scale bar = 5 µm. (C) Representative full field of view images taken for quantitation of SIFA of activated macrogametes in the transgenic 230Δ1314 and the parental line NF54/iGP2 lines stained with both anti-Pfs48/45 conjugated to 647 and anti-Pfs230 conjugated to 555. DAPI and merged images are shown. Scale bar = 20 µm.

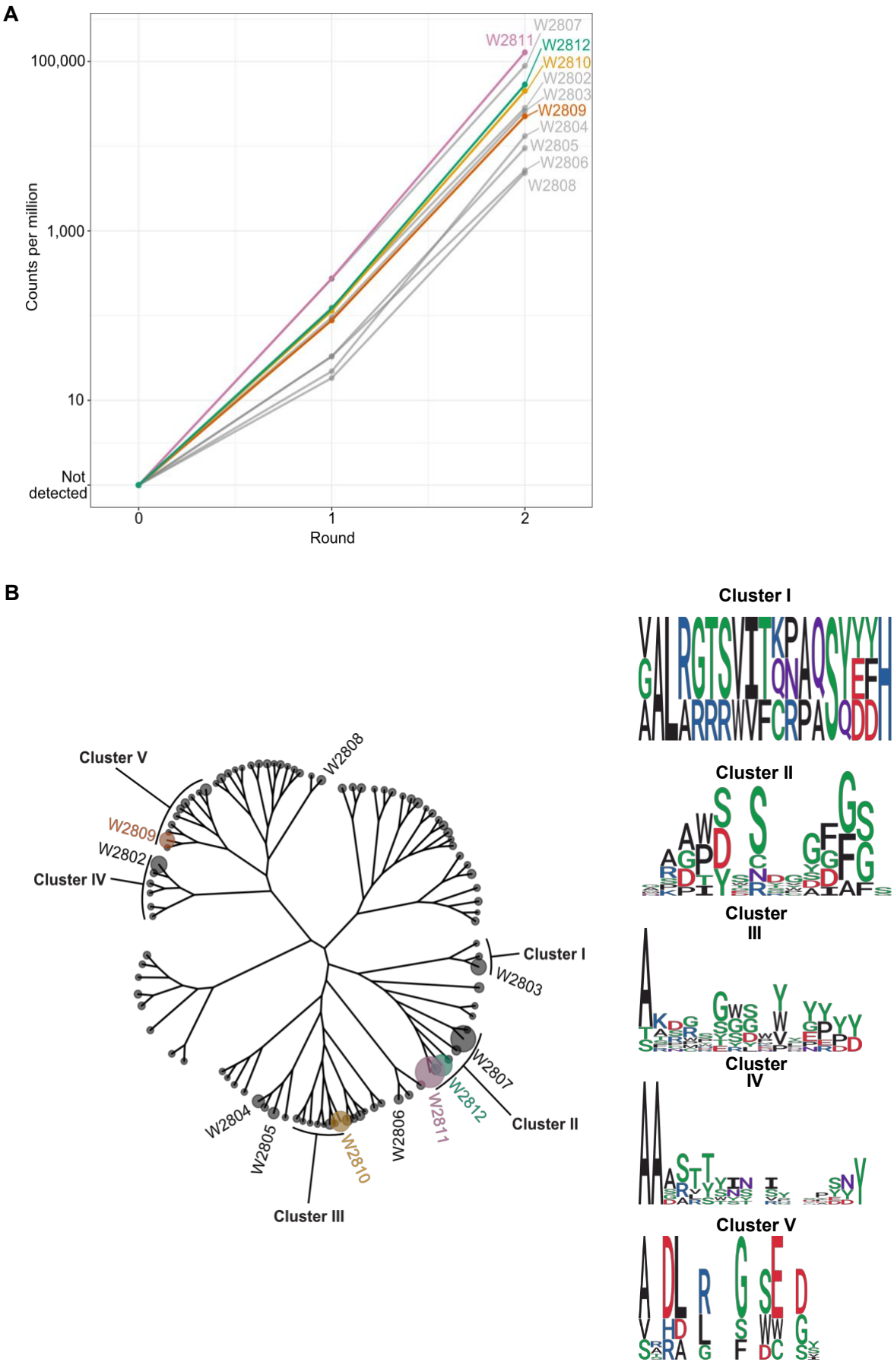

Figure S7. Next-Generation Sequencing analyses of Pfs230 D13D4 nanobodies phage display selection rounds. (A) Line graph of the normalized counts per million (CPM) of Pfs230 D13D14 nanobodies across the panning process. (B) Cladogram of the 100 most abundant nanobodies from Next-Generation Sequencing (NGS) after two rounds of phage display. Anti-Pfs230 nanobodies identified by Sanger sequencing are labelled. Tree tips are scaled relative to abundance (counts per million). Selected nanobody clusters (I to V) are highlighted and amino acid sequences of CDR3s in selected clusters of the cladogram are visualized as sequence logos.

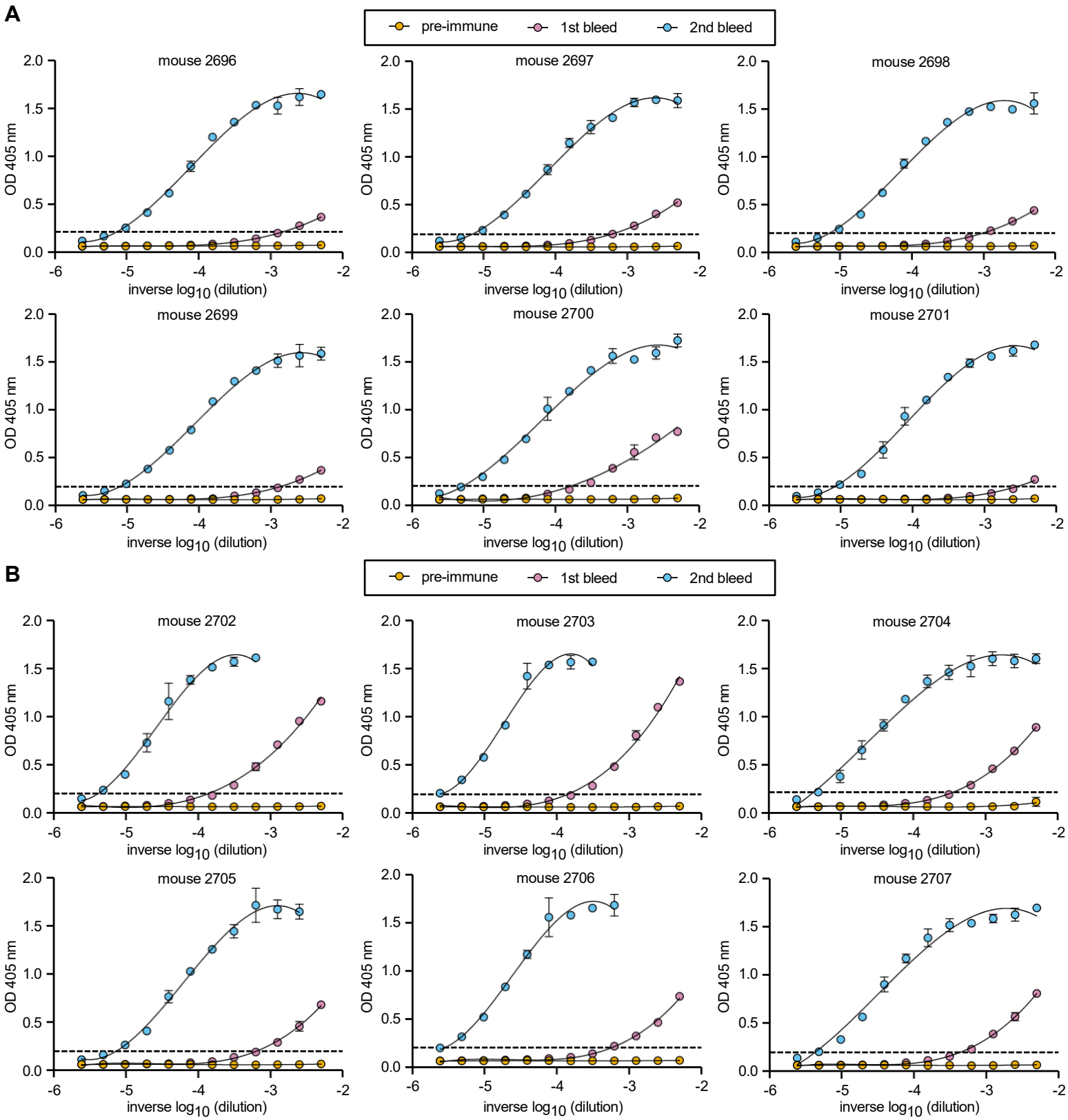

Figure S8. Immunization with Pfs230 D13D14 mRNA-LNPs elicited antibodies against Pfs230 D13D14.

(A) Sera of mice immunized with Pfs230 D13D14L mRNA-LNP and (B) Pfs230 D13D14S mRNA-LNP were serially diluted two-fold and binding to Pfs230 D13D14 was measured by ELISA. Serum dilution series was performed on pre-immune (orange), first bleed (pink) and second bleed (blue) sera for each mouse. Curves were fitted to a third order polynomial regression curve and outliers were excluded. The cutoff to determine endpoint titer is represented by the dashed line and was defined as three times the average absorbance values of the respective mouse pre-immune serum. Error bars represent standard deviation of the mean of two technical replicates.

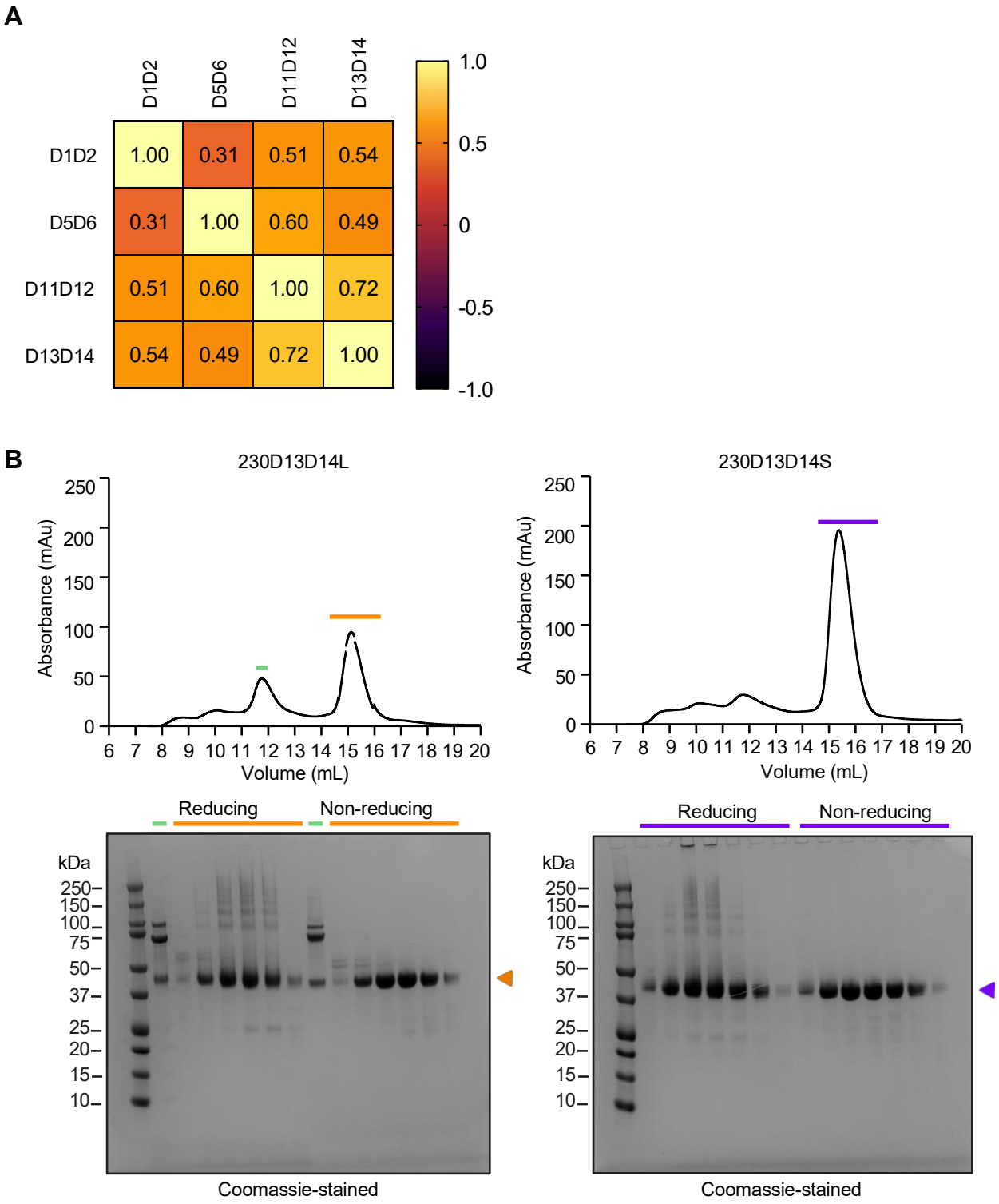

Figure S9. Cross-reactivity analyses of naturally acquired humoral immunity to Pfs230 domains and size exclusion chromatography for 230D13D14L and 230D13D14S proteins
(A) Spearman correlation of IgG antibody levels to the four different Pfs230 recombinant constructs shows mild correlation and provides limited evidence for cross-reactivity. (B) Size exclusion chromatography (SEC) profiles of affinity purified 230D13D14L (left) and 230D13D14S (right) from Sf21 insect cell expression. Coomassie-stained SDS-PAGE gel with fractions spanning the main SEC peak (15.3 mL elution volume) for monomeric 230D13D14L (orange line) and 230D13D14S (purple line). The higher molecular weight peak at 11.8 mL of potential protein aggregates (green line) is higher for the 230D13D14L SEC profile compared to that of the 230D13D14S profile. SDS-PAGE of this fraction (green line) also shows the presence of higher molecular weight entities.

Table S1 Cryo-EM data collection, refinement and validation statistics of endogenous Pfs230-Pfs48/45 complex

	Consensus map (EMD-48672) (PDB 9MVV)	Local refinement – Pfs230 D1-D8 (EMD-48669) (PDB 9MVT)	Local refinement – Pfs230 D9-14 and Pfs48/45 (EMD-48670)
	Composite map (EMD-48673)		
Data collection and processing			
Microscope	Titan Krios	Titan Krios	Titan Krios
Magnification	96,000	96,000	96,000
Voltage (kV)	300	300	300
Electron exposure (e^{-}/Å^2)	50	50	50
Defocus range (μm)	-0.4 to -1.6	-0.4 to -1.6	-0.4 to -1.6
Pixel size (Å)	0.808	0.808	0.808
Symmetry imposed	C1	C1	C1
Initial particle images (no.)	3,224,889	3,224,889	3,224,889
Final particle images (no.)	87,061	87,061	87,061
Map resolution (Å)	3.36	4.86	3.34
FSC threshold	0.143	0.143	0.143
Map resolution range (Å)	2.9-50.9	4.4-15.9	3.0-52.9
Refinement	*		
Initial model used (PDB code)	7ZXG, 7ZXF, AlphaFold2	AlphaFold2	
Model resolution (Å)	3.98	12.46	
FSC threshold	0.5	0.5	
Model composition	Pfs230 D9-D14 and Pfs48/45	Pfs230 D1-D8	
Non-hydrogen atoms	10,436	7,304	
Protein residues	1,394	1,471	
B factors (Å^2)			
Protein (min/max/mean)	30/ 294/ 104	30/ 791/ 396	
R.m.s. deviations			
Bond lengths (Å)	0.004	0.003	
Bond angles (°)	0.77	0.84	
Validation			
MolProbity score	1.74	1.73	
Clashscore	5.89	5.61	
Poor rotamers (%)	0.0	0.0	
Ramachandran plot			
Favored (%)	93.59	93.52	
Allowed (%)	6.41	6.34	
Disallowed (%)	0.0	0.14	

* EMReady map

Table S2. **Data collection and refinement statistics for Pfs230 D13D14-nanobody complexes.**

	Pfs230 D13D14 – W2809 (PDB 9E7N)	Pfs230 D13D14 – W2810 (PDB 9E7O)	Pfs230 D13D14 – W2812 (PDB 9E7P)
Data collection			
Wavelength	0.953732	0.953647	0.953728
Space group	$P4_3\ 2_1\ 2$	C2	$P4_12_12$
Cell dimensions			
a, *b*, *c* (Å)	79.9, 79.9, 342.7	135.5, 62.8, 56.5	134.4, 134.4, 75.6
α, β, γ (°)	90, 90, 90	90, 98.9, 90	90, 90, 90
Resolution (Å)	47.17-2.49 (2.64-2.49)	39.92-1.93 (2.05-1.93)	47.60-3.22 (3.41-3.22)
R_{meas} (%)	16.4 (232.4)	8.8 (136.4)	13.1 (147.0)
$CC_{1/2}$ (%)	99.9 (69.3)	99.9 (70.4)	99.9 (71.8)
I / σI	16.10 (1.50)	13.83 (1.48)	16.44 (1.77)
Total no. of reflections	1,062,054 (165,948)	248,059 (38,131)	157,102 (24,890)
Unique reflections	39,958 (6,222)	35,422 (5,608)	11,793 (1,841)
Completeness (%)	99.8 (98.7)	99.8 (98.9)	99.9 (99.7)
Redundancy	26.6 (26.7)	7.0 (6.8)	13.3 (13.5)
Wilson B ($Å^2$)	68	44	96
Refinement			
Resolution (Å)	47.17-2.49	39.92-1.93	47.60-3.22
No. reflections	39,948	35,377	11,747
R_{work} / R_{free}	22.4 / 26.4	21.4 / 25.4	28.6 / 32.0
No. atoms			
Pfs230	4,753	2,328	2,199
Nanobody	1,916	862	935
Small molecules	19	16	13
Water	62	128	
B-factors			
Pfs230	63	50	111
Nanobody	76	52	113
Small molecules	74	44	114
Water	56	46	
R.m.s. deviations			
Bond lengths (Å)	0.004	0.009	0.003
Bond angles (°)	0.67	1.03	0.60
Ramachandran plot			
outliers (%)	0.0	0.0	0.0
favored (%)	96.3	97.7	94.5
Rotamer outliers (%)	0.28	0.59	0.31
C-beta outliers	0.0	0.0	0.0
MolProbity score	1.42	1.40	1.82

For each crystal structure a single crystal was used for data collection. Values in parentheses are for highest-resolution shell.

R_{meas}, data redundancy-independent R-factor; $CC_{1/2}$, half-set correlation coefficient; $I/\sigma I$, intensity-to-noise ratio; R_{work}, refinement R-factor of work set; R_{free}, refinement R-factor of test set.

Table S3. Summary of interactions between Pfs230 D13D14 and nanobodies W2809, W2810 and W2812.

Interactions Pfs230 D13D14 – W2809 complex (PDB 9E7N): chain BD interface area 623 Å^2 / chain CA interface area 711 Å^2

Pfs230	Group	W2809	Location	Group	Distance (Å)
Hydrogen bonds					
Gln 2978	OE1	Arg 30	CDR1	NH2	2.4
Tyr 2980	O	Ser 56	CDR2	OG	2.6
Glu 2982	OE1	Ser 52	CDR2	OG	2.9
Glu 2982	OE2	Ser 54	CDR2	N	3.0
Glu 2982	OE1	Ser 54	CDR2	OG	2.6
His 2994	NE2	Asp 31	CDR1	O	2.8
Ser 2999	O	Gly 103	CDR3	N	2.9
Ser 2999	O	Gly 104	CDR3	N	2.9
Ser 2999	N	Gly 104	CDR3	O	3.1
Salt bridges					
His 2942	NE2	Asp 31	CDR1	OD1	2.9
Lys 2943	NZ	Asp 31	CDR1	OD1	3.3
Other interface residues in Pfs230					
Tyr 2940	Lys 2981	His 2984	Ser 2993	Phe 2996	Thr 2997
Tyr 2998	Lys 3000	Lys 3001	Cys 3010	Ile 3109	
Other interface residues in W2809					
Trp 53	Ile 57	Asn 74	Trp 100	Pro 101	Gly 102
Met 1105	Trp 106				

Interactions Pfs230 D13D14 – W2810 complex (PDB 9E7O): chain AB interface area 588 Å^2

Pfs230	Group	W2810	Location	Group	Distance (Å)
Hydrogen bonds					
Tyr 2879	OH	Asp 104	CDR3	OD2	3.4
Asn 2882	N	Ser 103	CDR3	OG	3.0
Asn 2882	ND2	Ser 102	CDR3	OG	2.9
Asn 2882	OD1	Ser 102	CDR3	N	3.1
Asn 2882	OD1	Ser 103	CDR3	OG	3.6
Val 2892	N	Ser 103	CDR3	O	3.1
Phe 2895	O	Tyr 105	CDR3	N	2.8
Salt bridges					
Lys 2900	NZ	Glu 44	CDR1	OE1	3.0
Lys 2900	NZ	Glu 44	CDR1	OE2	3.5
Lys 2931	NZ	Asp 104	CDR3	OD2	2.9
Lys 2931	NZ	Asp 104	CDR3	OD1	3.0
Other interface residues in Pfs230					
Pro 2880	Thr 2881	Glu 2883	Glu 2888	Asn 2889	Phe 2890
Phe 2891	Asn 2896	Leu 2897	Asn 2910	Asp 2922	Tyr 2924
Lys 2929	Leu 2955				
Other interface residues in W2810					
Ala 33	Phe 37	Phe 47	Ser 50	Ser 52	Gly 56
Ser 57	Ile 58	Arg 59	Pro 100	Tyr 101	Gly 106
Phe 108					

Interactions Pfs230 D13D14 – W2812 complex (PDB 9E7P): chain AB interface area 685 Å^2

Pfs230	Group	W2812	Location	Group	Distance (Å)
Hydrogen bonds					
Lys 2858	N	Asn 105	CDR3	OD1	3.0
Lys 2858	O	Ile 104	CDR3	N	3.1
Ser 2954	O	Ser 57	CDR2	OG	2.9
Lys 2959	NZ	Tyr 59	CDR2	OH	2.9
Gln 2962	O	Thr 109	CDR3	N	2.9
Gln 2962	O	Thr 109	CDR3	OG1	3.4
Asn 2963	OD1	His 106	CDR3	ND1	2.8
Ile 2964	O	Ile 107	CDR3	N	3.2
Ile 2964	N	Ile 107	CDR3	O	2.8
Tyr 2966	N	Asn 105	CDR3	O	2.4
Tyr 2966	OH	Ala 58	CDR2	O	3.2
Tyr 2966	O	Asn 105	CDR3	ND2	2.7
Other interface residues in Pfs230					
Leu 2897	Glu 2859	His 2860	Leu 2955	Leu 2957	Asn 2961
Ile 2965	Gly 2967	Asn 2968			
Other interface residues in W2812					
Leu 47	Thr 52	Arg 53	Ser 54	Val 56	Thr 102
Tyr 103	Tyr 108	Asn 110	Ser 112	Asn 113	

Table S4. Priners and synthetic DNA sequences, related to Figure 1 and Figure 3.

Priners		
Nane	**Sequence**	**Anplification product**
Pfs230FL 3:Flag-TwinStrepII genotyping		
(**A**) Pfs230 tag 5' int check F	GATGTACCTTCGAAAACTATAACAGC	5' integration check of tag 1253 bp
(**C**) FLAG int check R	TAATCCTTATCATCGTCGTCCTTG	
(**D**) hDHFR_1.2KOInt_F	CCGCTCAGGAACGAATTTAG	3' integration check of tag 2041 bp
(**B**) Pfs230 tag 3' int check R	CGAAGATGTGGAAGGACTC	
(**A**) Pfs230 tag 5' int check F	GATGTACCTTCGAAAACTATAACAGC	Over region which tag is inserted 1721 bp (wild type) 4817 bp (integrated)
(**B**) Pfs230 tag 3' int check R	CGAAGATGTGGAAGGACTC	
230Δ1314-3:Flag-TwinStrepII genotyping		
(**A**) Pfs230 5' int check F2	AAGTTACTGGAGATGAAACAGCTAC	5' integration check of D13D14 deletion/tag insert 752 bp
(**C**) FLAG int check R	TAATCCTTATCATCGTCGTCCTTG	
(**D**) hDHFR_1.2KOInt_F	CCGCTCAGGAACGAATTTAG	3' integration check of tag 2041 bp
(**B**) Pfs230 tag 3' int check R	CGAAGATGTGGAAGGACTC	
(**E**) 230-D13D14 WT check F	ATGTTACTACTAAAGTTGCTACTTG	Over the Pfs230 D13D14 coding sequence which is deleted 445 bp
(**F**) 230-D13D14 WT check R	CATCCATGAATTTCTTTATATCCTTG	
230Δ1314-3:Flag-TwinStrepII line generation		
230-D13D14-KO 5'HR F	GGTGCGGCCGCTCAAACAGAAATATTATTCATGG	Anplifies 498 bp of nucleotide sequence directly 5' of the K2828 Pfs230 Donain 13
230-D13D14-KO_5'HR R	GGTCTCGAGTTTTTCATCTATTTTTATTTTATCCATTGTAC	
Guide RNA target sequence		
Pfs230_g8947	ATTCATGGATGTGATTTCAC	
Recodonised Coding Sequence (Pfs230 CDS)		
Original sequence: TCATGGATGTGATTTCACAGGAAAATATTCCCATTTATTTACATATTCAAAAAAACCTTTACCAAATGATGATGATAT ATGTAATGTAACTATAGGTAATAATACATTCTCAGGTTTTGCATGCTTAAGCCATTTTGAATTAAAACCAAATAACTG CTTCTCATCTGTTTATGATTATAATGAAGCCAATAAAGTTAAAAAATTATTCGATCTATCCACAAAAGTAGAATTAGA CCATATCAAACAAAATACTTCAGGATATACACTATCATATATTATTTTTAATAAAGAATCCACAAAACTTAAATTCTC ATGTACATGCTCATCCAACTATTCAAATTATACTATACGAATCACATTTGATCCTAATTATATAATCCCAGAACCTCA ATCAAGAGCCATCATTAAATATGTAGATCTGCAAGATAAAAATTTTGCAAAATACTTGAGAAAGCTT **Recodonised sequence:** CCATGGCTGCGACTTTACTGGAAAATATTCCCACCTGTTCACCTATAGCAAAAAGCCGCTGCCGAACGACGA CGACATCTGCAACGTGACCATTGGCAACAACACCTTCTCCGGTTTTGCATGTCTGTCCCACTTTGAACTCAAG		

CCAAATAATTGTTTCTCTAGCGTCTATGATTATAACGAGGCTAATAAGGTGAAAAAGCTTTTCGACTTGTCGACCA
AAGTTGAGCTGGATCATATTAAGCAGAATACCAGCGGTTATACTCTGAGTTACATCATCTTTAACAAAGAGAGCA
CCAAGTTGAAGTTCAGCTGCACGTGCAGCAGCAATTACTCTAACTACACGATCCGCATTACCTTCGACCCGA
ACTACATCATTCCGGAACCGCAGAGCCGTGCGATTATCAAGTACGTTGATCTGCAAGATAAAAACTTTGCGAA
ATACCTGCGTAAATTG

gBlock DNA Synthesis

T7-priner-adaptors 3:Flag TwinStrepII (Restriction sites in bold, linker regions unnarked, as well as additional stop codons)

TAATACGACTCACTATAGGG**CTCGAG**GCAGCAGCCGACTACAAAGATGACGACGATAAAGATTACAAGGACG
ACGATGATAAGGATTATAAAGATGATGACGATAAGGCCGCAGCCTCAGCCTGGAGTCATCCACAGTTTGAGAA
AGGAGGTGGTAGTGGAGGAGGATCAGGTGGATCTGCCTGGTCTCATCCTCAATTTGAAAAATGATAATAG**CCC**
GGGCCGCTGAGCAATAACTAGC

Data S1. (separate file)

Excel file containing cross-linking mass spectrometry results and scan parameters, related to Figure 1.

Data S2. (separate file)

Data related to the Pfs230 nanobodies described in Figure 4. Table list nanobody sequences, ELISA reactivity to Pfs230 D13D14 and affinity measurements using BLI.